UNIVERSITY OF CALIFORNIA SAN DIEGO

Techniques in Optical Coherence and Resonance for Sensing

A dissertation submitted in partial satisfaction of the
requirements for the degree
Doctor of Philosophy

in

Electrical Engineering (Photonics)

by

Brandon John Sung Hyun Hong

Committee in charge:

Professor Yeshaiahu Fainman, Chair
Professor Richard Averitt
Professor Boubacar Kante
Professor Andrew Kummel
Professor Paul Yu

2019

The dissertation of Brandon John Sung Hyun Hong is approved, and it is acceptable in quality and form for publication on microfilm and electronically:

_____

_____

_____

_____

_____

Chair

University of California San Diego

2019

DEDICATION

This work is dedicated to my fiancée and family, who were there every step of the way.

TABLE OF CONTENTS

Signature Page . . . iii

Dedication . . . iv

Table of Contents . . . v

List of Figures . . . vii

Acknowledgements . . . viii

Vita . . . x

Abstract of the Dissertation . . . xi

Chapter 1 Introduction . . . 1
- 1.1 Surface plasmon resonance . . . 1
- 1.2 Optical coherence . . . 3
  - 1.2.1 Low-coherence interferometry . . . 3
- 1.3 Biosensing . . . 4
  - 1.3.1 Overview . . . 4
  - 1.3.2 Label-free detection . . . 4
- 1.4 Thermal infrared detection . . . 6
  - 1.4.1 Detection mechanisms and optical readout . . . 6
- 1.5 Spectroscopy . . . 8
  - 1.5.1 Stationary Fourier transform spectrometers . . . 8
- 1.6 Outline . . . 9

Chapter 2 Integration of Faradaic electrochemical impedance spectroscopy into a scalable surface plasmon biosensor for in tandem detection . . . 11
- 2.1 Introduction . . . 11
  - 2.1.1 Faradaic Electrochemical Impedance Spectroscopy . . . 12
- 2.2 Fabrication . . . 13
- 2.3 Experimental Setup . . . 16
- 2.4 Characterization . . . 17
  - 2.4.1 Surface plasmon resonance . . . 17
  - 2.4.2 Faradaic electrochemical impedance spectroscopy . . . 19
  - 2.4.3 SPR – f-EIS calibration . . . 20
- 2.5 SPR – f-EIS neutravidin immunoassay . . . 21
- 2.6 Discussion . . . 24
- 2.7 Conclusion . . . 26

Chapter 3 Simple nanoimprinted polymer nanostructures for uncooled thermal detection by direct surface plasmon resonance imaging . . . 27
3.1 Introduction . . . 27
3.1.1 Thermal properties and view factors . . . 28
3.2 Experiment . . . 29
3.2.1 Thermo-optic infrared sensing . . . 29
3.2.2 Thermal IR-SPR imaging . . . 34
3.3 Conclusion . . . 42

Chapter 4 Channel Dispersed Fourier Transform Spectrometer . . . 44
4.1 Introduction . . . 44
4.1.1 Principle of Operation . . . 45
4.2 Experiment . . . 47
4.2.1 Optical setup . . . 47
4.2.2 Results . . . 49
4.3 Discussion . . . 53
4.4 Conclusion . . . 55

Chapter 5 Surface Plasmon Resonance Profilometry and Dynamic Optical Patterning of Thin Liquid Dielectric Films . . . 56
5.1 Introduction . . . 56
5.1.1 Coupling of SPP into grating covered with dielectric . . . 60
5.1.2 Thin film equation for liquid deformation . . . 62
5.2 Results . . . 64
5.2.1 Numerical results of the resonant coupling angle as a function of liquid thickness . . . 64
5.3 Experimental setup . . . 67
5.4 Experimental results . . . 69
5.4.1 K-space imaging . . . 69
5.4.2 Real-space imaging . . . 70
5.5 Conclusion . . . 72

Bibliography . . . 74

LIST OF FIGURES

Figure 2.1: Illustration of SPR-EIS 14
Figure 2.2: Fabrication of SPR-EIS 15
Figure 2.3: Setup for SPR-EIS 16
Figure 2.4: SPR calibration for SPR-EIS 18
Figure 2.5: EIS calibration for SPR-EIS 20
Figure 2.6: SPR – f-EIS calibration for SPR-EIS 22
Figure 2.7: SPR – f-EIS immunoassay 23

Figure 3.1: Thermo-optic setup with SPR 30
Figure 3.2: Thermo-optic measurement with SPR 32
Figure 3.3: Fabrication of thermal-IR responsive SPR gratings 35
Figure 3.4: Spectral responsivitiy of IR absorbing coating 38
Figure 3.5: SPR imaging of single-pixel IR responsive gratings 40
Figure 3.6: Thermal sensitivity of SPR IR responsive gratings 41
Figure 3.7: Thermal isolation of pixels through focused ion beam milling 42

Figure 4.1: Experimental setup for the CDFTS 50
Figure 4.2: High pixel density recovery in CDFTS 51
Figure 4.3: Low pixel density recovery in CDFTS 52
Figure 4.4: Low pixel recovery of quantum dot spectra in CDFTS 54

Figure 5.1: Working principle for SPR profilometry of TLD films 59
Figure 5.2: SPP coupling relation for TLD film covered metal grating 61
Figure 5.3: Numerical relation between the resonant coupling angle and TLDF thickness 66
Figure 5.4: Experimental system for SPR topometry of TLD films 68
Figure 5.5: Experimental results of TLDF thickness measurements via k-space method. 70
Figure 5.6: Free surface deformation of TLDF imaged by SPR imaging method 71

ACKNOWLEDGEMENTS

I want to thank my advisor Yeshaiahu Fainman who has advised and encouraged me throughout my academic career. His insight, knowledge and good cheer were an indispensable motivator for my research.

I also want to thank my committee members, Professors Paul Yu, Richard Averitt, Boubacar Kante, and Andrew Kummel, who provided helpful feedback to guide my thesis work.

Many thanks to my colleagues Drs. Muhan Yang, Faraz Monifi, Felipe Vallini, Shimon Rubin and Lindsay Freeman whose collaboration, conversation and advice helped to turn difficult thought experiments into a reality. Many thanks to the members of the Ultrafast and Nanoscale Optics lab, whose talent, wisdom and good humor I could always count on.

Lastly, I want to thank my family for their immeasurable support throughout my academic career. Their patience and faith were a deep source of encouragement. Finally, I want to thank my fiancée, Joanna Wang: your love and support throughout my studies were a beacon of hope, and as constant as the sun, moon, and stars.

Chapter 2 is in full, a reprint from a manuscript published in Optics Express, 2015, Hong, Brandon; Sun, Alexander; Pang, Lin; Venkatesh, AG; Hall, Drew; Fainman, Yeshaiahu. The dissertation author was the primary author of this manuscript and Yeshaiahu Fainman was the principal investigator.

Chapter 3 is in full, a reprint from a manuscript published in Applied Material and Interfaces, 2017, Hong, Brandon; Vallini, Felipe; Fang, Cheng-Yi; Alasaad, Amr; Fainman, Yeshaiahu. The dissertation author was the primary author of this manuscript and Yeshaiahu Fainman was the principal investigator.

Chapter 4 is in full, a reprint from a manuscript published in Nature Communications Physics, 2018, Hong, Brandon; Monifi, Faraz; Fainman, Yeshaiahu. The dissertation author was the primary author of this manuscript and Yeshaiahu Fainman was the principal investigator.

Chapter 5 is taken from material submitted for review and publication, authored by Rubin, Shimon; Hong, Brandon; and Fainman, Yeshaiahu. The dissertation author was primary co-author of this manuscript with Shimon Rubin, and Yeshaiahu Fainman was the principal investigator.

VITA

2002	B.S. in Electrical and Computer Engineering, University of California, San Diego
2016	M.S. in Electrical and Computer Engineering, University of California, San Diego
2019	Ph.D in Electrical and Computer Engineering, University of California, San Diego

PUBLICATIONS

Shimon Rubin, Brandon Hong, Yeshaiahu Fainman, "Surface Plasmon Resonance Profilometry and Dynamic Optical Patterning of Thin Liquid Dielectric Films", *in review*, 2019.

Brandon Hong, Faraz Monifi, Yeshaiahu Fainman, "Channel dispersed Fourier transform spectrometer", *Communications Physics*, 1, 2018.

Brandon Hong, Felipe Vallini, Cheng-Yi Fang, Amr Alasaad, Yeshaiahu Fainman, "Simple nanoimprinted polymer nanostructures for uncooled thermal detection by direct surface plasmon resonance imaging", *ACS applied materials and interfaces*, 9, 2017.

Sung W Kim, Lin Pang, Brandon Hong, Joanna Ptasinski, Yeshaiahu Fainman, "Experimental demonstration of quenched transmission effect of an ultrathin metallic grating", *Optics letters*, 44, 2016.

Brandon Hong, Alexander Sun, Lin Pang, AG Venkatesh, Drew Hall, Yeshaiahu Fainman, "Integration of Faradaic electrochemical impedance spectroscopy into a scalable surface plasmon biosensor for in tandem detection", *Optics express*, 23, 2015.

John Hong, Edward Chan, Tallis Chang, Tze-Ching Fung, Brandon Hong, Cheonhong Kim, Jian Ma, Yaoling Pan, Rob Van Lier, Shen-ge Wang, Bing Wen, Lixia Zhou, "Continuous color reflective displays using interferometric absorption", *Optica*, 2, 2015.

ABSTRACT OF THE DISSERTATION

Techniques in Optical Coherence and Resonance for Sensing

by

Brandon John Sung Hyun Hong

Doctor of Philosophy in Electrical Engineering (Photonics)

University of California San Diego, 2019

Professor Yeshaiahu Fainman, Chair

Optical sensors are ubiquitous for their precision and non-contact acquisition, and have enjoyed widespread use in applications such as biosensing, environmental monitoring, and security. Despite their sensitivity, many of these sensors rely on costly laboratory instrumentation, and are not adaptable to the ever-growing volume of consumer detectors and optics that are readily available, making their application limited to benchtop analytics. This work leverages plasmonic resonances and optical coherence phenomena to make modifications upon traditional sensing formats that improve their sensitivity when deployed in off-the-shelf optical systems. In particular, we demonstrate that label-free plasmonic sensors can be combined with electrochemical impedance spectroscopic biosensors to tackle the problem of specificity in label-free sesning,

demonstrate the novel use case for the plasmonic detection of thermal infrared radiation, and show that plasmonic imaging is conducive to the characterization of nanometric thin liquid films. Moreover, we show that by introducing limited dispersion to Fourier transform spectroscopy, we can efficiently use camera detector formats and imaging systems to implement a high resolution scan-less Fourier transform spectrometer. By improving the figures of merit for sensor devices, we aim to translate traditional analytical sensing instrumentation from the laboratory benchtop into the consumer marketplace, and to spearhead a host of new applications.

Chapter 1

Introduction

This chapter will describe the motivation for developing sensor technology, define their contextual usage across a variety of applications, and briefly introduce the physics of optical resonance and coherence phenomena that drive modern optical sensors.

1.1 Surface plasmon resonance

Physically, surface plasmon resonance (SPR) is the resonant excitation of collective electron oscillations, plasmons, along a metal surface. Formally, the resonance is a guided electromagnetic mode confined to and propagating along the dielectric-metal interface. The resonant mode momentum is determined by the electromagnetic response of the interfacial materials, that is, their respective electric permittivities (under the assumption of non-magnetic materials). The dispersion relation describing surface plasmon polariton SPP modes is as follows:

$$k_{spp} = \frac{\omega}{c_o}\sqrt{\frac{\varepsilon_1\varepsilon_2}{\varepsilon_1+\varepsilon_2}}$$

where ω is the excitation frequency, c_o is the vacuum speed of light, ε_1 is the dielectric permittivity, and ε_1 is the metal permittivity, which is negative in its real part [Rae98]. Since the

electromagnetic mode profile evanescently decays from the interface into both interface materials, the modal effective index is exponentially more sensitive to changes in the permittivity that are closer to the surface. This sensitivity is leveraged in biosensing; by functionalizing the metal surface with ligands, surface captured biomarkers serve to strongly change the effective index of the SPP mode, and thus, measurably shift the resonance condition for coupling.

In the context of biosensing, optical excitation of SPPs is arguably the most commonly employed method of excitation [Hom03]. Owing to the boundary conditions of the dielectric-metal interface, SPPs can only be excited by radiation polarized in the plane of incidence, that is, with the magnetic field transverse (TM polarized). Radiative electromagnetic modes lack the intrinsic momentum to directly match the guided mode condition required for SPP excitation; (i.e. schemes with SPP modal interfaces that can be biologically functionalized) momentum matching schemes such as prism coupling or grating coupling must be employed [H.R13]. While evanescent prism coupling is efficient, the total internal reflection condition to be met for modal excitation requires large angles of optical incidence, making sensor geometries bulky and thus difficult, if not impractical, to scale. Grating-excitation of SPP is achieved by coupling evanescent diffraction orders of an incident optical wave into a metal film that is beneath the grating [HSD10], or is conformal to the grating itself [RAC$^+$68]. By using gratings of subwavelength periodicity, small incidence angle excitations of SPPs can be achieved, and scalability can be factored into sensor design.

To track the SPP resonance shift in response to surface binding events, we employ angular spectroscopy [aJH08], whereby a quasi-monochromatic source excitation is focused onto the functionalized metal grating surface, and projected in reflection onto a detector array. The appropriate cross section of the detector corresponds to an angular spectrum proportional to the numerical aperture of the focusing element, wherein momentum matching to the SPP mode is evident as a fringe-like resonant absorption of light. When using a grating coupler, this resonant angle is prescribed by the following grating equation:

$$\frac{\omega}{c_o}\sin\theta_i = k_{spp} + m\frac{2\pi}{\Lambda_g}$$

where m is an integer, θ_i the angle of incidence, and Λ_g is the grating periodicity [H.R13]. This resonant absorption is manifested as a symmetrically separated dark fringes, corresponding to positive and negative angles meeting the SPP mode matching condition for gratings.

1.2 Optical coherence

As an electromagnetic wave, light can be characterized by its polarization, amplitude and phase over space and time. Detectors are generally too slow to measure optical fields directly, and are responsive to the intensity of light. As such, measuring the optical field can be accomplished through the interference of a beam split and recombined colinearly with a mutual time delay implemented by an extended optical path in one arm. Scanning the delay in time, a temporal interference pattern of the signal is recorded on the photodetector. Similarly, interferometry can also be implemented by recombining the two beams with a non-zero interior angle, where the optical path difference is spatially implemented. In addition to being viewed directly on a scattering screen, the interference patterns can be recorded using a photodetector array or camera. In either case, the acquired interference patterns are the autocorrelation pattern for the measured source, and are related to the power spectrum by way of the Wiener-Khinchine theorem.

1.2.1 Low-coherence interferometry

Fourier transform spectroscopy involves the acquisition of a signal temporal coherence function and the computation of its corresponding Fourier transform in order to obtain the desired spectrum [GH07]. While a monochromator measures each resolvable spectral element with an acquisition duration sufficient to achieve a desired signal to noise ratio (SNR), the interferograms obtained in Fourier transform spectroscopy are a superposition of spectral elements, and for

equivalent acquisition times, will possess greater spectral SNR. Equivalently, monochromator-comparable spectral fidelity can be achieved from significantly shorter measurements. Fourier transform interferometers have established routine access to rapid and quantitatively precise infrared [FB12] and Raman [MRR07] spectra of materials for fundamental and applied studies of materials in physical, chemical, and biological domains. Its application has become indispensible in IR spectroscopy, where typical detectors for this region have not reached the low noise figures of their visible counterparts [GH07].

1.3 Biosensing

1.3.1 Overview

In the diagnosis of a disease, markers associated with the disease are typically found in the bloodstream in the form of proteins or other macromolecular structures. Biosensors in the form of immunoassays are designed with conjugate antibodies

1.3.2 Label-free detection

Label-free detection systems provide the rapidity of measurement required for the mobile deployment of a biosensor, while maintaining high sensitivity. A great number of label-free biosensors designed for immunoassays and disease detection have technologically matured over recent years. Among them include optical techniques such as surface plasmon resonance and waveguide sensing [Hom03, STK$^+$07], electrical techniques such as electrochemical impedance detection and FET-based gate sensing [aNP07, LKK09], and mechanical techniques such as stress-strain and dynamic resonance shift sensing [AMR11]. Such advances have been bolstered by the rapid progress in optical, electronic, and MEMS miniaturization and integration, and progress in their implementation as biosensors has consistently lowered limits of detection while maintaining

a minimalist protocol. The simplicity in these sensors suggest that label-free biosensors are amenable to mobile environments, where training and preparation are not prerequisites for use.

However, what the label-free systems gain in simplicity is lost in specificity. Real or human sampled biological fluids contain a plethora of proteins that interfere with the detection process, often in concentrations significantly higher than the target analyte. Label-free techniques must find a conjugate molecule specific enough to the target protein to make interferants negligible, or the raw sample must be stringently preprocessed to filter out competing biomarkers. In this manner, significant progress has gone into the careful and complex design of label-free immunoassays and associated protocols [pBH13]. However, the increasing complexity in this direction results in a higher bar to entry for rapid and mobile deployment of label-free biosensors. Even without non-specific interferants, the lack of labeling as an error-check belies the specificity of a biosensor that is sensitive to dynamic changes within the biological sample or instabilities due to environmental noise sources such as temperature (e.g., bulk refractive index changes for SPR).

Given the diversity of physical mechanisms currently employed for biosensing, the characteristics of multisensing, the integration of different sensors for the detection of a single analyte, have been investigated [Bre12]. Among these advantages include the reduction of label-free detection error (e.g., false positive/negative) rates by redundancy improved confidence intervals [KPRA14] and specificity improvements by physically orthogonal measurements without sacrificing individually characteristic sensitivities. Towards the latter, studies in the label-free multi-sensor integration of surface plasmon resonance and non-Faradaic electrochemical impedance spectroscopy have been conducted, via the plasmonic-EIS detection (p-EIS) scheme [LWW$^+$12, PDG$^+$14]. In the p-EIS modality, the non-Faradaic electrochemical impedance is coupled to the optical signal as an AC modulated SPR resonance and is extracted from the optical reflection by lock-in detection, while the DC, or drift, response characterizes the SPR resonance.

1.4 Thermal infrared detection

The infrared (IR) optical spectrum offers unique access to physical processes otherwise invisible to the naked eye. Measurements in this band have proven fruitful in their diverse applications, including the acquisition of characteristic chemical vibrational spectra for scientific and medical analysis, optical data transfer and telecommunications, and thermal imaging for military and civil service [VM10, RA12, BA02, Rob91, YY06, NSB$^+$10]. With thermal IR radiation emitted by many terrestrial objects centered in the 8-14 μm band as gray body radiators (objects with imperfect blackbody emissivity), detection and imaging within this spectral band is fundamental to remote sensing in low-light or obfuscating environmental conditions [Hol00]. Since their conception, IR detector sensitivity, bandwidth and form factor have been improved tremendously, with fast, sensitive and affordable IR imagers becoming increasingly market-competitive [Rog11].

1.4.1 Detection mechanisms and optical readout

Many mechanisms for IR detection have been explored and characterized. Photon detectors based on both intrinsic and extrinsic band-gap carrier generation have been well characterized as IR detectors and focal plane arrays with high sensitivity [VM10, Rog11, Rog03]. However, their performance is contingent upon low device temperatures maintained by cryogenic cooling [VM10], rendering such detectors inseparable from accompanying refrigeration units. Thermal IR sensors leveraging thermoelectric, pyroelectric, and bolometric effects have been developed and have enjoyed significant commercial success [Kru01]. By the absorption of incident radiation, thermal detectors measure the effect of induced temperature shift by voltage generation against a junction thermal reference (thermoelectric effect), induced ferroelectric voltage (pyroelectric effect), or a thermal shift of electrical resistance (bolometric effect). Generally, performance in these detector elements are limited by their heat transfer characteristics, which affect the specific

detectivity, and time response of the developed thermal sensor. Consequently, a drawback for thermal sensors is the high thermal conductance of silicon upon the read-out integrated circuit (ROIC) that limits the maximum temperature contrast achievable, where contact to the ROIC substrate must be limited by employing multi-step etch processes to suspend the sensing thermal element by narrow legs which also function as electrical leads for sensing [VM10].

A solution to this issue is developing thermal IR sensing based on the temperature induced change of the material optical properties to leverage the improvements made in the sensitivity of optical detection technologies. Crucially, thermo-optic IR sensors employ an optical read-out system and do not require integrated design of a thermal focal plane array into a ROIC substrate plane. Sensors based on MEMS bimorphs [JBR$^+$09, TFTU09, SCR$^+$03], photonic crystals [EPL$^+$13], bio-inspired reflectors [PUS$^+$12], low dimensional materials such as graphene [QHL$^+$16] and integrated optical components [ZOY14] have been investigated. A significant advantage claimed for optical readout in thermo-optic IR sensing is the dispensation of an ROIC, minimizing or complete eliminating the need for electrical contact [Ost06]. Readout mechanisms can be made independent of the substrate, conferring a design freedom for thermal isolation unique to an ROIC-independent platform, also enabling parallelism provided by imaging over the sensor array.

Besides thermal management and parallelism, the absorption of existing thermal detectors have been enhanced through plasmonics [ZYC12, YZR$^+$14] - by resonantly interacting with a metallic nanostructure the incident infrared radiation is more strongly absorbed to the near-field, thereby improving the efficiency of the absorption cross-section for the infrared sensor architecture. While plasmonic devices have been employed to improve light collection efficiency, it is well known that plasmonic modes are sensitive to the thermo-optic properties of the dielectric interface in which the mode is supported [TS03, CCW$^+$07].

1.5 Spectroscopy

Spectroscopy, the measurement of weighted frequency content in optical signals, is a precise method of characterizing the interaction of light with matter. This characterization spans the entire electromagnetic spectrum, and in optics, is employed in the visible, infrared, and terahertz domains. For a light source with a known spectrum entering a port in an optical system, missing bands in the exiting probe spectrum can be identified to infer system absorption, reflection, scattering, and fluorescence; these measurements can characterize the system material and interferometric properties. In addition to taking a ubiquitous role in the natural sciences as a probe of atomic and molecular structure and dynamics on nearly every material scale, spectroscopy can be found in numerous technological applications as a remote sensor, in medical devices [ZIM+13], agricultural and industrial monitoring [RSA11], and interferometric and hyperspectral imaging [IKH16]. For a signal of a given strength and bandwidth, the quality of a spectroscopic measurement is a function of the probing instrument, or spectrometer, and can be described by its signal strength over noise, minimum resolvable feature, and photometric accuracy [SOKH08]; the importance of eah figure of a merit is dependent on the application (e.g. chemical band identification can prioritize the distinguishability of two closely spaced spectral bands over the quantitative accuracy of their respective amplitudes while sensing applications require precise detection of small changes in an absorption or scattering peak) [FSPF16].

1.5.1 Stationary Fourier transform spectrometers

The in situ detection of trace features of analyte in a complex environment requires an accurate sensor capable of measuring low levels of indicator signal in real time, and with limited capability for sample filtration, must resolve signal traces with specific discrimination from background markers. Optical spectroscopy excels at chemical identification and is ubiquitous in the sciences as a highly specific and noninvasive probe of molecular structure [HF06, MRR07,

BB15, HML17, RLSC13, RASC14, FSPF16]. In Fourier transform (FT) spectroscopy, the high signal throughput has proved a boon to overcoming the difficulties of otherwise overwhelming detector noise in infrared spectroscopy and near-infrared Raman spectroscopy, and is desirable for in situ measurement [GH07, Bak14, MR08, FB12, SOKH08]. In contrast with benchtop mirror-driven spectrometers, stationary FT spectrometers utilize multichannel detector arrays to record spatial interferograms for spectral recovery [AOA$^+$16, Coa07], and while favorable for in situ FT spectroscopy, the fixed length of the detector array and pixel size fundamentally limit their spectral resolving power.

Stationary interferometers, in which the same interference is spatially dispersed to form a pattern measured by a detector array [AOA$^+$16], have been developed towards removing the kinetic scanning element of the system design [Coa07]. This interferometer scheme is conducive to compact system designs and confers rapid measurement owing to the parallelism of the optical path delay measurements. For designs using common optical paths [Bar85], interference measurements are stable owing to the rigidity of the optical axes. Moreover, stationary interferometers leverage the significant advances made in increasing the pixel density and photometric accuracy of detector arrays, both quantum and thermal, across the visible, NIR, and IR spectra.

1.6 Outline

The dissertation is structured as follows:

In Chapter 2, the design of a sensor integrating two label-free biosensor formats is presented. In particular, an SPR immunoassay biosensor is integrated into a planar electrode geometry to simultaneously with an electrochemical impedance spectroscopic (EIS) immunoassay. This work uses information published in *Optics Express*, 2015, Hong, Brandon; Sun, Alexander; Pang, Lin; Venkatesh, AG; Hall, Drew; Fainman, Yeshaiahu.

In Chapter 3, a novel demonstration of SPR detection of thermal infrared radiation is

presented. Using the thermo-optic (TO) effect, thermal-infrared radiation absorbed by the high TO coefficient material cladding the SPR supporting surface induces an index shift that can be measured by resonance tracking of the SPR. This work uses information published in *ACS Applied Materials and Interfaces*, 2017, Hong, Brandon; Vallini, Felipe; Fang, Cheng-Yi; Alasaad, Amr; Fainman, Yeshaiahu.

In Chapter 4, a modification to the stationary Fourier transform spectrometer by introducing dispersion is presented. By introducing dispersion, sampling constraints imposed by using only one dimension (1D) of the camera array are lifted, and the limiting resolution can be improved beyond the resolution limits of a 1D detector array, towards the full pixel count of a 2D camera array. This work uses information published in *Nature Communication Physics*, 2018, Hong, Brandon; Monifi, Faraz; Fainman, Yeshaiahu.

In Chapter 5, the application of SPR imaging for thin liquid dielectric films is presented. For liquid layers thinner than the optical wavelength, the overlap of the interface within the evanescent field of the SPR mode is sensitive to small changes in interface height by its pronounced effect on the effective refractive index supporting the guided resonance. In particular, the ability to accurately characterize the surface of liquid interfaces on a sub-nanometric scale is shown. This work uses information currently under review, authored by Rubin, Shimon; Hong, Brandon and Fainman, Yeshaiahu.

Chapter 2

Integration of Faradaic electrochemical impedance spectroscopy into a scalable surface plasmon biosensor for in tandem detection

2.1 Introduction

In this paper, we detail the design and characterization of integrating SPR and Faradaic EIS (f-EIS) onto a single transducer substrate as uncoupled and non-interfering measurements. Given the aim for such a system to impart practicality as a mobile biosensor, we present a design for our integrated system that considers eventual compacting of the device by allowing for scalability. Our concern is in developing a multisensor device platform that can be used both as a multisensor with error-checking redundancy and a platform for the study of physical orthogonalities between SPR and f-EIS measurements, as it applies towards reducing the associated uncertainty of complex biological fluids. We therefore seek to demonstrate that SPR and f-EIS can be integrated as

individually functional immunoassay detection systems, without loss of sensitivity in either modality. Towards this end, we experimentally show that in our integrated multisensor, the respective interrogation of SPR or f-EIS does not interfere with the other, and demonstrate the corroboration of multimodal measurements in a neutravidin-capture immunoassay, for low concentrations.

2.1.1 Faradaic Electrochemical Impedance Spectroscopy

Electrochemical impedance spectroscopy (EIS) is the measurement of the electrical impedance across an electrochemical cell, which is typically composed of an ionic solution in between two metal electrodes. As in Fig. 2.1(a), small sinusoidal voltage signals, usually with less than 10 mV amplitudes, at multiple frequencies ranging from 0.1 Hz to 100 kHz are applied between the electrodes and the resulting current response for each frequency is used to produce an impedance spectrum. By fitting this spectrum to well-studied circuit models that describe the different electrical mechanisms of the cell, physical and chemical effects that alter these electrical characteristics can be determined (Fig. 2.1(b)). While this type of modeling of electrochemical cells is employed in many different fields, among which battery design is prominent [AMS+11], EIS is well characterized in its use as a sensitive label-free biosensor that does not perturb the biomolecular films that develop on the electrodes with the higher voltage signals typical of other commonly used electrochemical sensing techniques [aIW03].

Two variants are often employed: non-Faradaic and Faradaic EIS. The former method, which ideally has no electron transfer between the electrodes, focuses on measuring the so-called double layer capacitance created by the formation of ions and charged molecules near the electrode surface. Hence, physical displacement of these charges produce a change in the dielectric properties of the electrode-solution interface thereby altering the double layer capacitance. In the context of biosensing, EIS can be used to interrogate the binding of biomarkers to functionalized ligands on the surface of the electrodes by measuring the value of this capacitance. The latter

variant, Faradaic-EIS (f-EIS), hosts the analyte in a buffer containing a high concentration of a reversible reduction-oxidation (redox) molecular pair in order to deliberately introduce electron transfer with the electrodes via electrochemical reactions driven by the applied voltage signal. In this case, the electrical component of interest is the resistance created by the redox molecules reacting and transferring electrons, also known as the charge transfer resistance (Rct). Any changes on the surface that impede or discourage the probability of the molecule undergoing redox reactions, such as immunoassay binding events that block the surface of a functionalized electrode, will increase this resistance. Hence, as in Fig. 2.1(b), detection is measured by the increase in charge transfer resistance extracted from the spectroscopic data, according to the following impedance model:

$$Z(\omega) = R_s + \Big(\frac{1}{(j\omega)^m C_{dl}}\Big) || \Big(R_{ct} + \frac{R_W}{(j\omega)^{0.5}}\Big)$$

where ω is the frequency in radians per second, R_s is the solution resistance, m is the phase parameter, C_{dl} is the double layer capacitance, R_W is the Warburg resistance, and $||$ indicates the equivalent parallel impedance. While there is still some variation in the double layer capacitance in this version of EIS, the magnitude of the impedance change due to the charge transfer resistance overshadows the signal from dielectric fluctuations.

2.2 Fabrication

Thin film gold gratings with optically sub wavelength periodicity were patterned into coplanar electrodes onto a silicon substrate (see Fig. 2.2). To electrically isolate the electrodes from the silicon substrate, 1 μm of PECVD grown SiO_2 (Oxford Plasmalab PECVD) was deposited on the bare substrate, then diced to sample size. To pattern the optical grating, 400 nm of AZ1505 resist was spun onto the substrate, then UV holographically exposed and developed to form photoresist gratings with a 1D quasi-sinusoidal profile (owing to the nonlinear dosage curve)

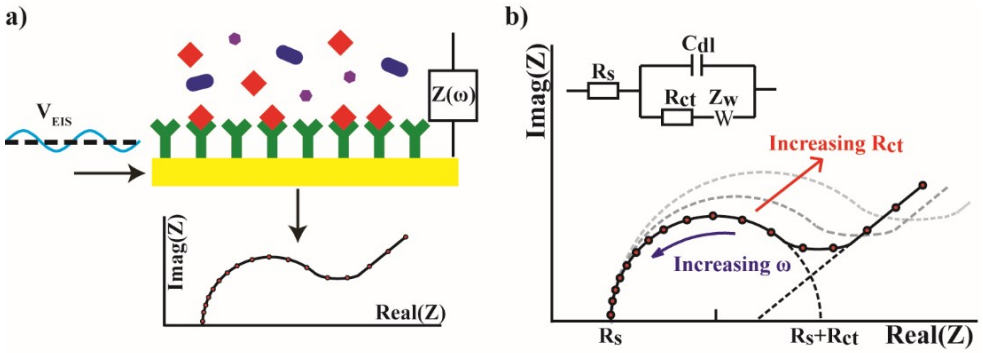

Figure 2.1: EIS works by applying a small voltage signal across the electrodes in an electrochemical cell and measuring the generated current signal as the frequency of the excitation signal is varied to produce an impedance spectrum similar to the ones shown in the Nyquist plots above (a). In f-EIS, the binding events from a label-free immunoassay increase the charge transfer resistance (R_{ct}) of the electrochemical cell by blocking the redox molecules from reacting with the surface. R_{ct} is calculated by fitting the impedance spectrum to Randles Circuit model shown in (b). Visually, an increase in R_{ct} can be seen in the Nyquist plot as an increase in the radius of the semicircle portion of the curve.

with appx. 570 nm periodicity, as measured by SEM (Philips XL30 ESEM). Eight gratings were patterned per sample, for future multispot detection. The sample was then hard-baked at 120^o C for 30 min to confer mechanical stability to the resist, which remains as part of the final structure. A plastic shadow mask was then cut to form 30 mm by 2 mm electrodes (Silhouette Portrait vinyl cutter) with 1 mm coplanar gap, long edge running parallel to the grating wave-vector. The choice in gap reflects a design to maintain low electrode capacitance and reduce electrical modulation in the surface plasmon signal [FST08]. Finally, in order of deposition, 10 nm of SiO_2, 5 nm of Ti and 75 nm of Au are sputtered (Denton Discovery 18) through the shadow mask to complete both plasmonic transducer and electrode as in Fig. 2.2. The intermediate 10nm of SiO_2 is sputtered to assist eventual PDMS bonding and protect the underlying resist from mechanical wear and blocking it from fluidic analyte. Thicknesses were measured using a combination of stylus profilometry (Dektak 150 surface profiler) and ellipsometry (Rudolph Auto EL Ellipsometer). For microfluidics, PDMS molds with 0.1 mm by 50 mm parallel channels were

fabricated according to previously reported methods [LCG$^+$06].

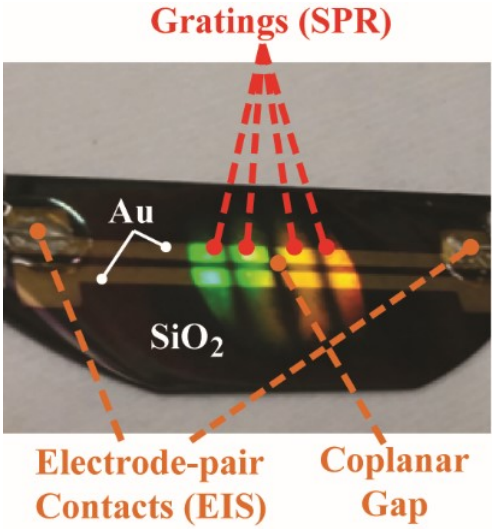

Figure 2.2: The SPR - f-EIS transducer substrate overlays a gold electrode pattern onto a holographically exposed glass/resist film stack. The periodicity of the plasmonic grating was determined by the grating equation and numerical calculation for a design minimizing the excitation angle for a 785nm source at a gold-water interface (n = 1.33), while avoiding the poor plasmonic coupling efficiency of near-normal incidence excitation brought on by standing wave formation. The thickness of the gold was experimentally swept from 20 nm to 200 nm to maximize efficiency at the designed excitation angle. Good absorption contrast was found for 75 nm of gold, which is necessary for sensitive centroid detection. Each grating area is roughly 1 mm in lateral width, and are spaced 2 mm apart. Co-planar electrodes are paired length wise (the longer length of the substrate), and form a 1 mm gap. The overlap between the electrode and the grating form the interrogation area for SPR and f-EIS. Microfluidic channels from the PDMS chip are mounted parallel to the grating-electrode, and overlap a pair and corresponding gap. The optical beam is cylindrically focused to a vertical line with respect to the image.

Having fabricated the coplanar grating-electrodes, silver conductive epoxy was applied to bond external wire leads to the sample electrode contact pads, and cured at 65^o C, for 15 min (MgChemicals 8331, 17 mΩ-cm). A secondary nonconductive epoxy was overlaid to impart mechanical stability to the conductive bond.

2.3 Experimental Setup

To develop and test a robust system that could be compacted and scaled in size while preserving sensitivity, surface plasmon angular spectroscopy was chosen for its high tolerance for alignment error and simple normal incidence angle interrogation geometry. A 18 mW 780 nm centered LED (Thorlabs LED780E), bandpassed to 3 nm spectral FWHM (Semrock Line filter 785 nm) is used as the source to excite surface plasmons on the grating. An LED was chosen over a diode laser in order to remove coherent speckle interference, an artifact of coherence that is severely intolerant of system instability and detrimental to sensitivity [LGH$^+$14]. The diverging beam is collimated, passed through a polarizer, and focused by a cylindrical lens onto the grating, through the mounted PDMS. Collimated light fills the cylindrical objective lens, corresponding to a positive angular half-bandwidth of 14.25 degrees (28.5 degrees total bandwidth, centered at 0 degree normal incidence).

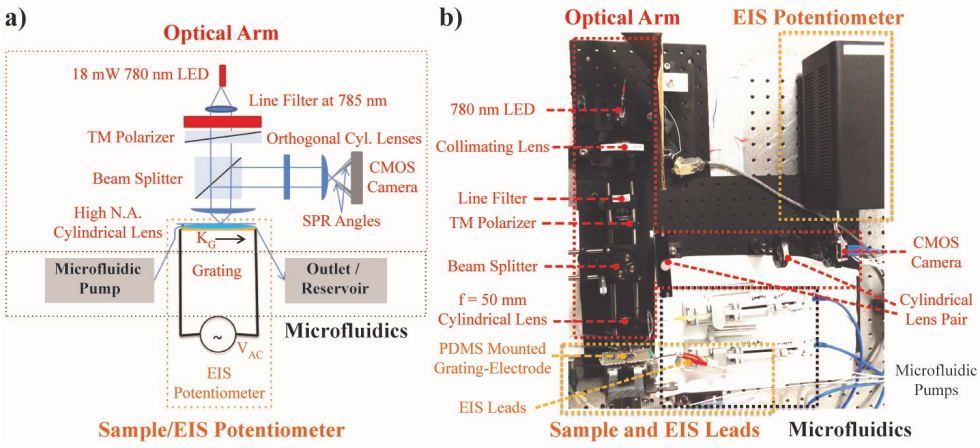

Figure 2.3: The system was designed for scalability; that is, the optical path geometry is rectangular, with orthogonal incidence and propagation angles, evident in the schematic (a). In the physical implementation (b), the sample (top, orange) is mounted at the end of the optical arm (red), and an impedance potentiometer (bottom, orange) is attached to the sample via leads (top, orange). Two fluidic pumps (black) drive an SPR - f-EIS channel and an SPR-reference channel.

To excite SPPs, both the incident polarization and grating wave vector lie in the plane of incidence spanned by the cylindrically focused beam (i.e. the electric field is parallel to the

sample grating wave vector). The reflected signal is collected by the cylindrical interrogation objective, and passed through a beam splitter to the imaging arm. The imaging arm is comprised of two perpendicular cylindrical lenses along the same optical path. The lens with curvature in the plane of incidence re-projects the angular spectrum (i.e. spatial Fourier transform of the objective collected signal), while the lens with curvature out of the plane of incidence images the fluidic channels, with magnification (focal lengths 40 mm and 120 mm, respectively). A 1.3MP, 6x4.8 mm sensor CMOS camera with 3.7 μm square pixel size is placed at the imaging plane, and the Fourier transforming lens is placed appx. 10 mm from the imaging plane such that the angular spectrum spans the CMOS camera (eCon See3Cam 12CU NIR).

For the EIS, a commercial benchtop potentiostat (CHI 750E) was used by tying the counter and reference electrodes together and attaching them to one side of the gold electrode via the epoxied wire. The opposite wire was attached to the working electrode treating the sensor as a two electrode electrochemical cell. In future implementations, this device can easily be shrunk to a much smaller size. A PDMS microfluidic chip was then bound to the functionalized grating-electrodes, and two microfluidic channels were overlapped respective grating-electrode pairs and centered on their gaps. Interrogation light through the cylindrical objective lens was focused to a line perpendicular to the running fluidic channel length. With a microfluidic channel length of 5 mm, width of 0.1 mm, and an electrode gap of 1 mm, the overlap of the fluidic channel over the electrodes for f-EIS was appx. 0.4 mm^2.

2.4 Characterization

2.4.1 Surface plasmon resonance

To calibrate and examine the fidelity of the SPR component of the SPR-EIS system, we performed bulk refractive index detection tests using stepped concentrations of ethylene glycol, diluted with water. A concentration ladder of ethylene glycol was flowed through the microfluidic

channel over the grating-electrode surface at 40 μL/min, stepped from 0% (water) to 6% ethylene glycol. A reference channel of water at the same flow rate is measured over a second channel (not shown). The physical units of sensor response in angular (a 3.75 μm width pixel) resonance position are reported in response units (RU), in which the unit RU corresponds to the limit of detection 3σ, where σ is the measured signal standard deviation at steady state. This 3σ figure is a measure of noise in centroid position having a strong dependence on intensity contrast and system quality, such as camera shot noise and environmental temperature. A calibration sensogram obtained of the signal channel with reference channel subtraction, is shown in Fig. 2.4; the 1 RU point indicates a limit of detection of 0.1% glycol, corresponding to a bulk refractive index limit of detection of approximately 9 x 10^{-5} RIU. This matches well to previously reported thermal limit for a surface plasmon detector without temperature control [HPM^{+}08].

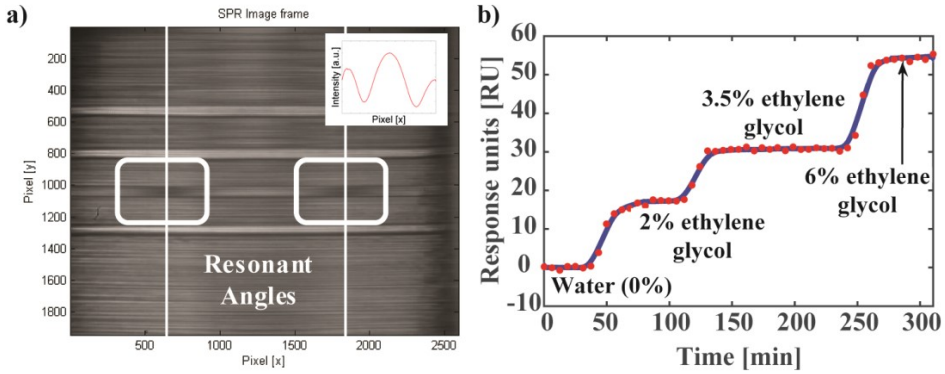

Figure 2.4: The full angular spectrum ($\pm 14^{o}$) afforded by the objective and projected onto a 3.75 μm pixel camera is shown (a) with evident SPR excitation fringes for diluted ethylene glycol (second channel from the bottom). The inset shows a length-wise cross section of the channel representing the angular absorption spectrum. The faint fringes outside the channels correspond to partial SPR excitation for the PDMS/gold interface. Since the cylindrical curvature of the lens is in the lateral direction (x), only the vertical (y) direction can be resolved as an image by an imaging cylindrical lens. The SPR excitation angle is tracked (b) for a ladder of ethylene glycol dilutions (right) and the extracted 3σ limit of detection for bulk refractive index change is 9 x 10^{-5} RIU.

The channel is the subimage region of interest, and represents the angular spectrum spanning its length (with normal incidence at the aperture center) and redundant across the channel width, up to noise. This region of interest is a matrix with entries according to single

exposure intensities at the corresponding subimage pixel. If we identify the channel length pixels of length L as the ROI columns, and the channel width W as the rows, we can obtain a 1D angular spectrum by computing the intensity sum of the matrix along the ROI rows to obtain a 1 x L angular spectrum vector. The centroid can be calculated by computing the intensity-weighted average of the pixel position, normalized to the total intensity across the vector; this is formally identical to calculation of the center of mass for a distributed body. Thus, as the fringe moves, the centroid will be displaced, providing an experimental sensor measure that is proportional to angle shift.

2.4.2 Faradaic electrochemical impedance spectroscopy

To verify the functionality of the f-EIS segment of the system, both cyclic voltammetry (CV) and EIS measurements were performed with different concentrations of the redox probe potassium ferro/ferri-cyanide in the same phosphate buffer saline (PBS) solution. For each measurement, the buffer solutions spiked with varying redox probe concentrations from 125 to 1000 μM were flowed through the microfluidic channel over the gold electrodes at 40 μL/min. For CV, the voltage was scanned from -0.4 to 0.4 V at a scan rate of 100 mV/s. As shown in Fig. 2.5(a), the resulting voltammograms appear similar to those of microelectrodes and show, as expected, that the peak current increases with increasing redox molecule concentration.

For EIS, the frequency is swept from 10 Hz to 10 kHz using an amplitude of 5 mV. The radius of the semicircle of the Nyquist plots (Fig. 2.5(b)) decrease with increased concentration. Hence, the charge transfer resistance decreases with higher concentration of the redox probe, since a larger presence of the charge carrier at the electrode surface increases the current. Both these trends match with the previously recorded results.

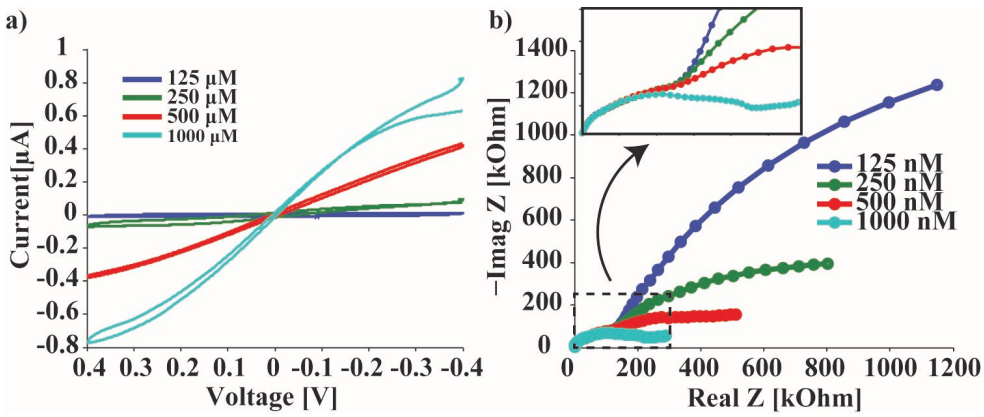

Figure 2.5: Voltammograms measured with CV (a) and EIS spectrum (b) made with the Ferro/Ferri solutions in the microfluidic channel.

2.4.3 SPR – f-EIS calibration

A necessary condition for effectual multisensor redundancy towards detection error reduction is the non-interference or independence between the measurements of each component sensing modalities. Separate calibrations of a multisensor baseline were performed to characterize the effect of one modality on the other. Specifically shown in Fig. 2.6 are baseline measurements of both SPR resonance angle, without and under f-EIS interrogation, and f-EIS charge transfer resistance, without and under SPR interrogation. In both cases, each measurement exhibits no detectable drift in its baseline, regardless of tandem interrogation by the second modality. Over the f-EIS baseline trend (Fig. 2.6(a)), the deviation in the mean charge transfer resistance between solo and tandem measurements is 0.11 Ω, within the acquired limit of detection (3σ) which was measured to be as narrow as 0.59 Ω. Over the SPR baseline (Fig. 2.6(b)), the maximum deviation in the SPR mean angle between solo and tandem measurements is 0.1 pixel, within the acquired limit of detection (3σ) which was measured to be as narrow as 1.4 pixels. This indicates that both f-EIS and SPR baseline responses during the multisensor measurement process remain well within the limit of detection characterized by respective solo measurements; no false positive/negative can be induced by error propagation through correlated sensor transduction mechanisms. This is a necessary condition for employing multimodal sensors towards redundancy, for detection

error reduction. Aside from the variability of binning statistics, we mention that a possible physical cause for fluctiation in the SPR limit of detection (standard deviation) is a previously demonstrated modulation of SPR on a high capacitance electrode surface by AC modulation of the surface charge density [FST08]. While this scheme (called p-EIS) leverages the high capacitance in order to transduce non-Faradaic electrochemical impedance measurements from the modulated SPR signal, our design intentionally aimed to minimize this effect and decouple the measurement processes by maintaining wide coplanar electrode gaps for minimal electrode capacitance. For our integrated grating-electrode system, SPR signal frames are acquired every 5 seconds, and since the f-EIS modulation exceeds 10 Hz, modulatory effects on the SPR would be severely aliased and would be detected as an increase in the SPR 3σ figure. Critically, the detectability of this effect is dependent on the efficiency of surface charge modulation, specifically the effective cell capacitance, which is determined by the electrode geometry, cell and double-layer film capacitances. As our design employs wide gap coplanar electrodes and the electrochemical modality is the faradaic type with significant charge transfer, the SPR variance does not noticeably change between the absence and application of electrochemical interrogation. We emphasize that the limits of detection (3σ) for both individual and tandem baselines clearly remain well within the same order of magnitude, indicating sensitivity preservation in our multisensor.

2.5 SPR – f-EIS neutravidin immunoassay

Avidin proteins bind specifically to biotin, are well characterized, and are frequently used to test the surface sensitivity of an immunoassay-based biosensor design. Neutravidin, a deglycosylated complex of avidin, was chosen for its stability and neutrality in the electrochemical buffer used for our experiments [WDBW^{+}06, NSC12]. Prior to mounting the microfluidic PDMS, the sample was subject to 1 mM KOH / H_2O_2 cleaning, rinsing by deionized (DI) water, and careful drying. To form a functionalized monolayer on the grating-electrode surface, 100 μM

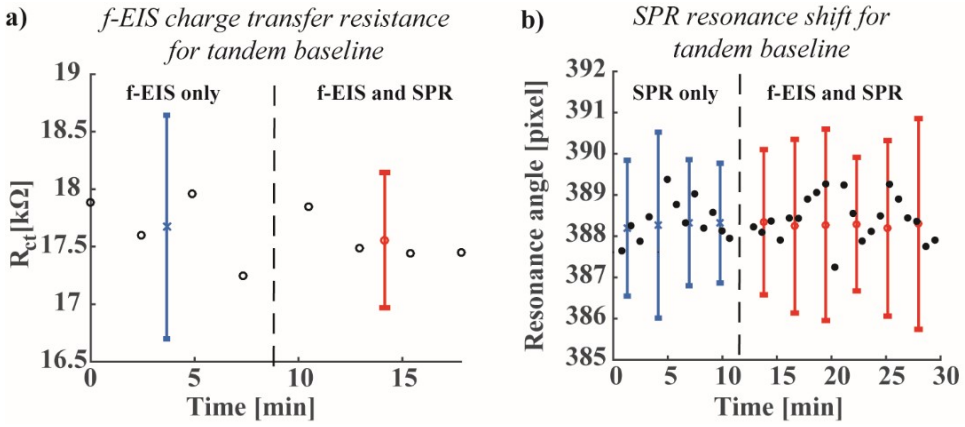

Figure 2.6: Tandem f-EIS - SPR baseline measurements to calibrate mutual interference. (a) An EIS baseline for charge transfer resistance (black) was obtained with the means and 3σ (limit of detection) for both resistance without (blue) and with (red) SPR interrogation. (b) An SPR baseline for resonance angle position (black, sampled for clarity) was obtained with running means and 3σ for both angle without (blue) and with (red) f-EIS measurement.

thiolated-biotin reagent solution (ethanol solvent) was incubated over the gold surface, in a closed environment for 1 hour (Sigma Aldrich Biotin-SAM formation reagent). A final phosphate buffer solution wash was performed.

Using two PDMS microfluidic channels for two respective grating-electrodes, the tandem SPR – f-EIS measurements were performed on one grating, while the second channel was employed as a reference channel for SPR. Using a microfluidic pump, all fluidic flow rates through the channel were set at 50 μL/min. Having previously determined the appropriate redox couple (ferro/ferri-cyanide, $K_4[Fe(CN)_6]$) / ($K_3[Fe(CN)_6]$) concentration by earlier calibration, 1 mM ferro/ferri-cyanide in PBS buffer was flowed over the biotin functionalized surface for approximately 20 min. The transient rise in the first 10 min is indicative of residual salt removal from the cleaning process and surface stabilization of the biotin monolayer, and the zero response unit (origin) is set to the steady state baseline.

After baseline stabilization, serial injections of decade stepped (10 nM to 1 μM) neutravidin concentrations in matched buffer (1 mM ferro/ferri-cyanide PBS) were performed. For each concentration, microfluidic pump controllers were programmed to inject 700 μL at the given flow

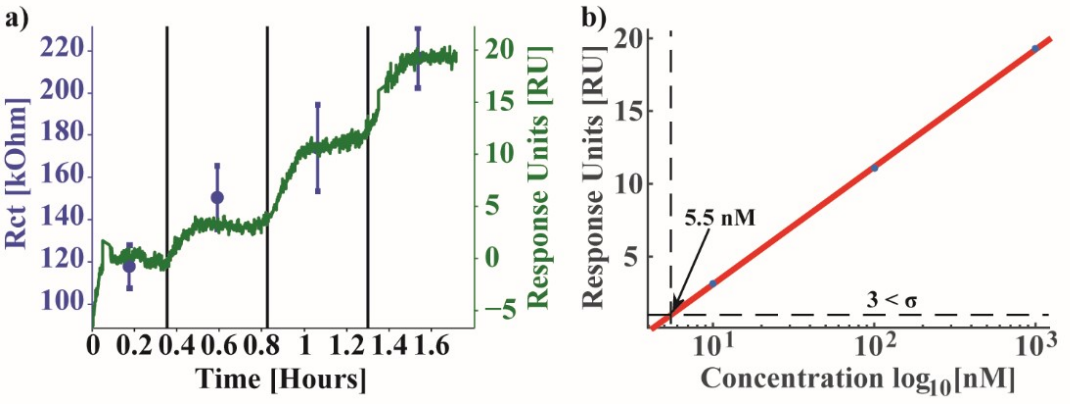

Figure 2.7: (a) Neutravidin immunoassay sensogram for tandem SPR - f-EIS measurements. f-EIS sweeps for 3 min with 2 min waiting intervals, and SPR measurements are taken appx. every 5 seconds; SPR (green) and f-EIS (blue) detections of neutravidin capture clearly corroborate by relative signal amplitude change. The initial transience at 10 nM is due to residue removal and stabilizes to equilibrium after appx. 10 min. (b) Semi-log equilibrium binding response curve for SPR shows limit of detection (3σ) to be appx. 5.5 nM.

rate, resulting in approximately 14 min of constant flow throughout each injection step. Given an inlet tubing length of approximately 200 μL in volume, at the given 50 μL/min rate, there is an approximately 4 min delay before the given bulk concentration of neutravidin, in microfluidic laminar flow, reaches the grating-electrode surface for binding detection. The dual signal responses, charge transfer conductance in EIS and resonant angle decrease in SPR (normalized to an increase in response units), are shown to sharply change in response to neutravidin capture by the biotin film; both responses reach equilibrium before the flow rate cessation, at appx. 10-12 min after binding begins. Prior to the subsequent injection step, a cessation of flow is briefly maintained to ensure steady state.

The disparity between the number of measurements reflects the physical disparity between both detection processes: f-EIS requires a steady state response for each spectrum comprising its chirped signal to accurately measure the cell impedance, while SPR extracts resonance position per pixel frame, and is limited by the camera frame trigger and image processing rate. This reveals an important aspect behind the integration of f-EIS, which is detailed in the Discussion section. Referring to Fig. 2.7(a), the 10 nM neutravidin capture is clearly resolved, and estimates

for LOD (3σ) based on a logarithmic calibration curve can be estimated (Fig. 2.7(b)), indicating a limit of detection of 5.5 nM for SPR and 10 nM for EIS. Sensitivity can be improved in the future, with steps taken towards improved temperature stabilization, source power tracking, and appropriate electronic filtering.

2.6 Discussion

In addition to creating an integrated multi-sensor with practical fabrication techniques and a scalable setup, our goal in this work was to demonstrate tandem detection on the same analyte, without loss of individual signal fidelity or sensitivity in each modality. Our analysis lies in the comparison of individually relative detection responses, and a mapping between charge transfer resistance and surface refractive index change is scaled such that the correspondence between relative amplitudes of f-EIS and SPR neutravidin detection is evident (Fig. 2.7(a)). Having demonstrated mutual non-interference between f-EIS and SPR detection schemes in our integrated biosensor, close agreement between the two modalities as to the kinetics and equilibrium of neutravidin capture is expected. A semilogarithmic relationship (lin-log) between SPR/f-EIS signals and neutravidin concentration is evident (Fig. 2.7(b)), which agrees with the characteristic equilibrium concentrations obtained in binding kinetics for a given analyte concentration. Furthermore, the individual sensitivities of f-EIS and SPR are clearly preserved, and agree with previously reported work on the stand-alone modalities [HPM$^+$08, OOW$^+$13, BLB$^+$13, QWC10]. Tandem non-interfering detection on the same analyte, without loss of individual signal fidelity or sensitivity in each modality, allows for redundancy to be implemented, imparting greater immunity to detection errors that are typically associated with truly label-free methods. Essentially, when the modalities are decoupled, the likelihood of failure in redundant detection due to single modality failure is the significantly lower likelihood of simultaneous failure.

The sparsity of measurements in the f-EIS signal as compared to SPR is a direct consequence of accurately measuring electrical impedance, which requires the chirped signal run long enough to resolve the steady-state impedance at each frequency being measured. In contrast, the SPR signal is acquired at a rate limited only by the exposure and image processsing time for each acquisition of the angular spectrum. However, this draws attention to the depth of f-EIS spectra, which is of particular interest to us. Specifically, the extraction of charge transfer resistance from the impedance spectrum represents a reduction of f-EIS spectrum to a single detection value, that is, a reduction in dimensionality. While this is sufficient for stand-alone f-EIS sensors, a motivation for designing this multisensor platform is to accurately explore the extraction of other electrochemical parameters characterizing the f-EIS spectrum such as solution resistance and diffusion impedance, as they compare to the single dimensional SPR response. Our future studies will investigate this relationship and how specificity might be gained by the SPR - f-EIS platform.

Several prior works in the plasmonic-EIS detection scheme (p-EIS) have thoroughly investigated and leveraged electrical modulation of SPR on an electrode for the simultaneous optical readout of electrochemical current, where the demodulated steady state optical signal is the SPR response. Coupling sensors in this format has the advantage of reducing the detection system to an all-optical format. However, critical sensing advantages are afforded to decoupled sensors, including the separation of sensor-specific noise figures (e.g. drift) and the preservation of individual sensor performances. Such a system provides greater fault tolerance by signal redundancy, reducing the prediction errors from limitations in the receiving operator characteristic (ROC) to which label-free sensors are particularly prone. Moreover, array processing of multisensor signals to improve analytic specificity requires minimal mutual dependence between the sensing modalities, such as electrochemical signal dependence on the physical efficiency of SPR modulation.

2.7 Conclusion

We have demonstrated the design and fabrication of a compact grating-electrode device for integrated and tandem surface plasmon resonance and Faradaic electrochemical impedance spectroscopic biosensing. Furthermore, by detection of neutravidin capture by a functionalized biotin film on this device, we have experimentally verified that the tandem measurement process is uncoupled, and maintains independent functionality for each of the two modalities while preserving the high sensitivities characteristic to each detection scheme. Our future work aims to use this decoupled biosensor scheme to study how the physically different the sensing mechanisms can be leveraged towards reducing the dimensionality in sensor response to complex fluids and improve the specificity of label-free biosensors. By way of the scalable design of substrate and setup, investigation in the aforementioned direction will enable improvements in the specificity of label-free biosensors.

This chapter is in full, a reprint from a manuscript published in Optics Express, 2015, Hong, Brandon; Sun, Alexander; Pang, Lin; Venkatesh, AG; Hall, Drew; Fainman, Yeshaiahu. The dissertation author was the primary author of this manuscript and Yeshaiahu Fainman was the principal investigator.

Chapter 3

Simple nanoimprinted polymer nanostructures for uncooled thermal detection by direct surface plasmon resonance imaging

3.1 Introduction

Surface plasmon resonance (SPR) sensing confers a narrow Lorentzian shape resonance [PHSF07, TPF06] for highly sensitive resonance shift detection that is uniquely sensitive to refractive index changes in low dimensional film profiles owing to its evanescent transverse mode profile. This modality has enjoyed significant success in biosensing, with high sensitivity to refractive index changes in nanometer-scale biofilms and protein interactions, and the capability for highly parallel and real-time grid readout as an optical imaging modality [HYG99, Hom03, HPM$^+$08]. Transitively, the localized sensitivity of SPR is highly amenable to the detection of IR induced thermo-optic changes in the local refractive index of thin IR sensitive films [YZR$^+$14].

In this manuscript, we experimentally demonstrate the uncooled detection of long-wave infrared (LWIR) radiation by thermal surface plasmon sensing, using an all optical read-out format. The SPRs are employed to detect the IR induced temperature change, leveraging the high sensitivity of the tightly bound mode profile to refractive index changes in a low-profile thermal mass. By depositing a thermal IR sensitive material onto a metallic grating, IR induced temperature changes in the refractive index via the thermo-optic coefficient are then measured as shifts in the SPRs. A demonstration of the thermo-optic shift is first presented as a response to the absorption of thermal infrared light in a glassy silicon nitride layer, as a proof of concept. We then change from a continuous grating to discrete and spatially resolvable SPR grating pixels of 500 x 500 μm^2 area fabricated by nanoimprint lithography for IR detection by SPR imaging. Having demonstrated the thermo-optic action of IR absorption in the dielectric cladding on SPR, polymer parylene-C is chosen as the grating pixel cladding layer for its high thermo-optic coefficient. Thermal IR detection in SPR imaging is experimentally measured with two thermal sources of different temperatures in order to extrapolate a system limit of detection. Design outlooks for performance based on pixel delimitation are also presented towards affordable room temperature high sensitivity thermal detection.

3.1.1 Thermal properties and view factors

Fundamentally, thermal infrared detection can be described as the measurable increase in temperature of a thermal mass due to the absorption of radiant infrared energy. The one-dimensional heat conductance equation describes the temperature dynamics of a thermal mass in response to the continuous absorption of thermal radiation:

$$C\frac{dT}{dt} + GT = \alpha P(t)$$

where T is the temperature over time of the thermal slab, C is the slab heat capacity, G

is the heat conductance connecting the slab to an environmental heat sink, and α describes the fractional power absorbed from incident radiant flux $P(t)$, under the assumption of ideal slab emissivity [VM10, Kru01]. When a shutter is opened to expose the thermal mass to the radiant flux from a thermal source, the intercepted exitance can be expressed as $P(t) = P_o u(t)$ where $u(t)$ is the unit step function and P_o is the steady state radiant exitance. The temperature step response is then $T(t) = T_O(1 - e^{-t/\tau})$ where $\tau = C/G$ is the characteristic time constant, and $T_o = \alpha P_o/G$ is the steady state temperature; the step response to a closing shutter is linearly related and can be similarly derived. It can then be understood that for sensitive and fast thermal infrared detectors, excellent thermal insulation by materials with low thermal conductivity are necessary for large temperature contrast, while small element sizes with low specific heat capacity maintain short time constants.

3.2 Experiment

3.2.1 Thermo-optic infrared sensing

An experimental setup was devised to observe the thermo-optic shift in the surface plasmon resonance induced by optical absorption in a bulk infrared absorbing dielectric cladding. Of particular interest was the evaluation of the first-order temperature step response to the radiative heat transfer from a thermal infrared source, and to characterize the optical readout sensitivity of a SPP resonance shift in the visible domain.

The measurement setup consists of two independent opti-cal paths for respective infrared thermal sensing and opti-cal readout, Fig. 3.1(a). To demonstrate the collection of IR emission from a thermal source, a silicon nitride furnace igniter at 1300^o C is imaged by a ZnSe f/2 optic with f = 6.24 cm (Thorlabs) in a 2f system (relay) configuration onto the SPR supporting grating device at an angle of approxi-mately 20^o from the surface normal. A reflective metallic shutter is placed between the optic and the source to regulate the thermal infrared flux from the source

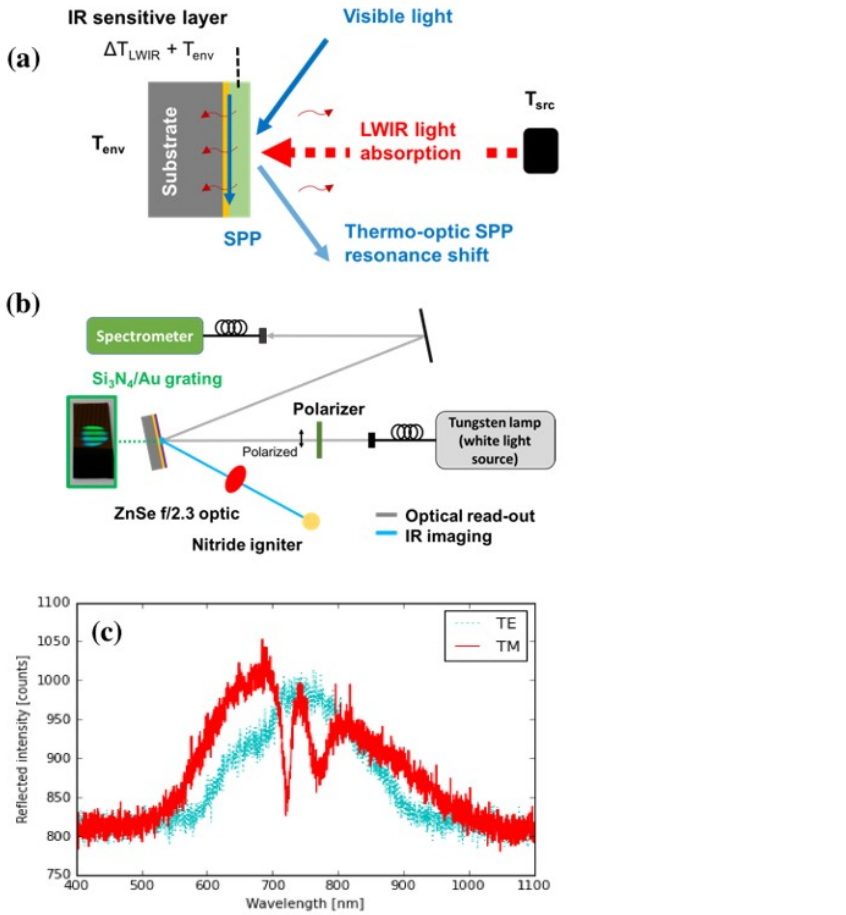

Figure 3.1: The thermo-optic detection of LWIR radiation measures temperature dependent visible light transmission or reflection from an IR absorbing system (a). Measurement setup (b) with thermal imaging relay system (blue) and visible readout optical components (gray). As in (c), light polarized in the plane of incidence (transverse magnetic, TM) couples into surface plasmon polaritons (SPP) while light polarized perpendicularly (transverse electric, TE) does not couple. Two resonant absorptions are visible, indicating that multiple grating orders satisfy the grating assisted phase matching for SPR excitation.

to substrate. The visible spectrum optical readout originates from a fiber coupled broadband tungsten lamp source of unpolarized white light that is subsequently collimated and polarized in the plane of incidence, spanned by the grating surface and normal to the grating wavevector, for transverse magnetic (TM) polarization. The polarized light is incident upon the SPR grating at an angle of approximately 10^o with respect to the grating surface normal. At the fixed incidence angle, select bands within the collimated broadband source that scatter from the grating are resonantly phase-matched to the SPR mode and absorbed. Non-resonantly reflected probe light then passes through the remaining optical path by a series of mirrors and into a Thorlabs reflective fiber collimator, which couples the signal to a UV-NIR spectrometer (Ocean Optics HR2000 UV-NIR).

To fabricate the plasmonic IR sensing device illustrated in the inset of Fig. 3.1(b), an AZ1505 photoresist layer is spun onto a silicon substrate to a 400 nm thickness, UV holographically exposed and developed into quasi-sinusoidal grating with 570 nm periodicity, followed by sputtering of 5 nm of adhesion titanium and 75 nm of gold (Denton Discovery 18). The fabrication procedure for the metallized gratings employs similar methods and instrumentation as previously reported [HSP$^+$15, PNF03]. An IR absorbing layer is developed by sputtering 200 nm of silicon nitride (Si_3N_4) onto the SPP grating layers; IR absorption in the thermal 8-14 μm spectral band is verified by Fourier transform infrared spectroscopic (FTIR) measurement in attenuated total internal reflection (ATR) (ThermoFisher Nicolet). By ellipsometric measurement, the refractive index of the silicon nitride layer was measured to be approximately 1.91 for 632.8 nm wavelength light.

Fig. 3.1(c) shows the reflected intensity for TM and TE polarizations. Since the incidence angle of the readout light is fixed in this configuration, refractive index changes in the absorbing layer are detected as spectral shifts of the reso-nant band, owing to changes in the phase matching condition at the fixed angle. In spectral readout generalized to Fig. 3.1(a), the use of broadband SPP resonance interrogation provides a large dynamic range defined by spectrometer and source

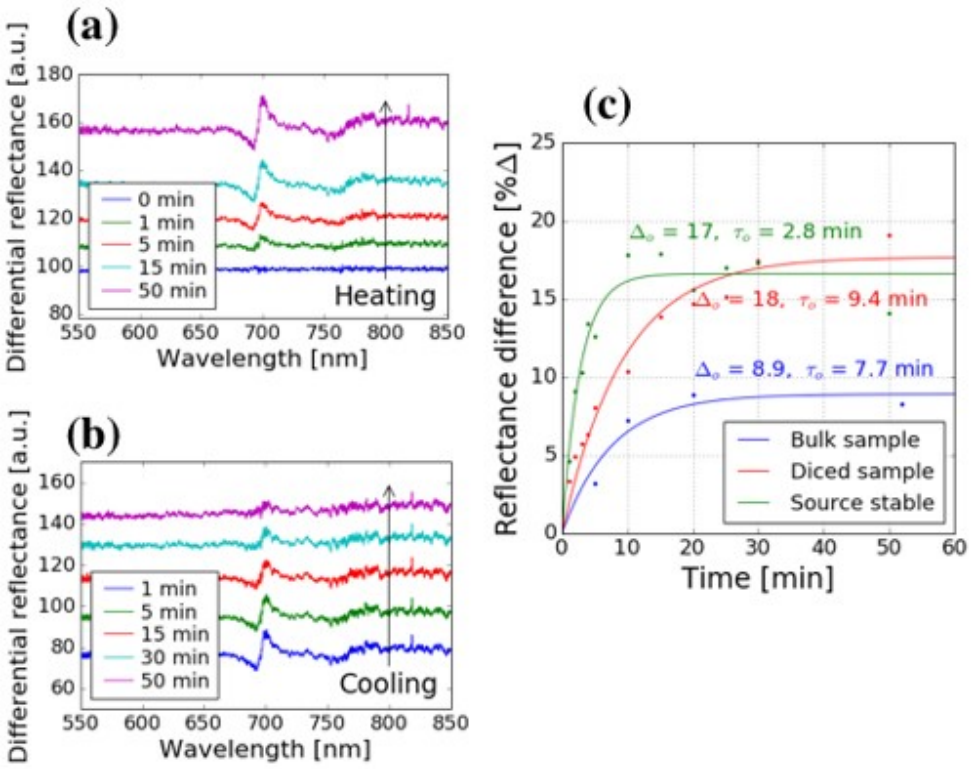

Figure 3.2: Thermo-optic SPP resonance blue-shift induced by absorption of IR light from thermal source (a) and redshift towards the baseline after shutter closure (b). Time response of the SPP sensor on a bulk substrate and for an identical sensor diced to the dimensions of the imaged source (c) such that the imaged radiant exitance is closely matched to the de-limited sensor dimension. For the delimited sensor (red), a significant increase in the steady state thermal shift is observed compared to the bulk sensor (blue), indicative of a decrease in the thermal heat conductance, while the proportionally smaller increase in the time constant owes to the reduced size of the film as well as the smaller heat capacity. The characteristic time constant of the detector is measured upon opening the shutter after heating the thermal source to its steady state (green).

spectral range [PHSF07], allowing for the fixed setup to accommodate the selection of IR sensitive materials with different refractive indices without experimental setup variation. For the silicon nitride film refractive index, the grating equation (2) can be solved to show that at the fixed incidence angle the positive second order evanescent diffraction mode is phase matched to the SPP resonance. Hence, increases in the dielectric refractive index serve to blue-shift the spectral SPR resonance. Optical paths for thermal infrared signal and visible optical readout were made coincident onto the SPR sensor area by aligning the visible image of the thermal source and the readout light onto the same area. As the thermal radiation was incident upon the sensor substrate at a more extreme angle, detectable scatter radiation did not couple into the visible readout path. This independence was verified by continuous spectrometer readings without the readout beam, with source alternately shuttered and exposed, without detectable perturbation to the measured readout spectrum.

Upon thermal IR absorption by the transducer silicon nitride film, the surface plasmon resonance spectral peak could be observed to shift, indicating a refractive index change due to the heating in the infrared absorbing nitride cladding film. The shift was quantified by taking a baseline spectrum with the thermal source removed, and subtracting it from subsequently obtained spectra over time; the absolute difference in the two peaks of maximum and minimum spectral intensity represents the differential shift in the surface plasmon resonance. As the sensor substrate is exposed to the thermal source, the imaged infrared radiation is absorbed by the SPP resonance supporting dielectric layer, inducing heating at the interface and throughout the bulk film. This temperature increase can be observed in Fig. 3.2(a) as a blueshift in resonance coupling wavelength, indicative of a positive thermo-optic effect in the dielectric interface coefficient ε_1 as dictated by both SPP resonance and momentum matching equations (2-3). Similarly, switching off the thermal source results in a decrease of radiant flux upon the sensor, and a cooling redshift can be observed in Fig. 3.2(b) as the source and substrate thermalize to the environment. Illustrated in Fig. 3.2(c), the characteristic first order time response to heating can be observed. After a

period of sustained exposure to the thermal source, the spectral blue-shift of the resonant input wavelength was observed to asymptotically cease; the equilibrium spectral shift from the baseline and rise time then characterize the substrate for the imaged source.

For each bulk and diced sample, the thermal source was brought from room temperature to steady state with the shutter open, and imaged continuously onto the detector substrate. Compared with the sensor on bulk substrate, the diced sample showed a significantly larger thermo-optic shift, blue and red curves in Fig. 3.2(c). Since the imaged source occupies only a fraction of the area of the bulk sample, delimiting the sensor area to dimensions that fall within the bounds of the thermal source image significantly reduces the heat conductance to the substrate while retaining the net radiant exitance delivered to the substrate; as per equation (3), this yields a larger thermo-optic shift. While the reduced thermal contact to the mount generally yields a larger time constant, the sensor delimitation also decreases the heat capacity of the silicon nitride film, and only a 22% increase in the time constant is observed. Finally, the rise time of the igniter thermal source itself was accounted for by allowing the source to ramp for 10 min with the shutter closed, and subsequently opening the shutter for imaging. Measuring the diced sensor response, the time constant, now restricted to the intrinsic device properties, is reduced by a factor of 2.75, from 9.4 min to 2.8 min, shown in the green curve of Fig. 3.2(c).

3.2.2 Thermal IR-SPR imaging

Having demonstrated the SPP resonance sensitivity to thermal infrared absorption, a method for multiplex division was sought. A well-reported advantage of optical readout of IR detection is the parallelism afforded by im-aging the sensor array [WO14]. By imaging the thermal source onto the sensitive image plane, the spatial distribution of the infrared radiance imaged across the array can be detected as the effects of localized heat transfer on the optical properties of the imager, as measured by a probing light source. In particular, when an SPP resonance supporting substrate is illuminated by a probe beam fixed in incidence near the resonant

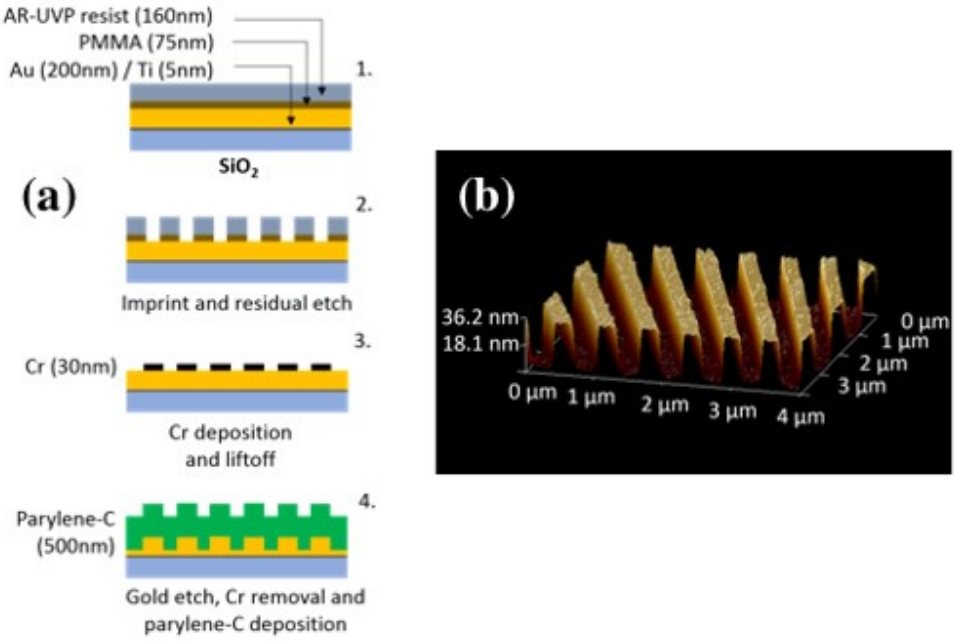

Figure 3.3: Nanoimprint fabrication process (a) begins with a Au-metallized borosilicate substrate for the spinning (1) and imprinting (2) of a bilayer AR-UVP / PMMA polymer stack. Cr mask transfer by liftoff (3) is performed for direct RIE etching into the gold for (4) subsequent deposition of 500 nm IR sensitive parylene-C in a furnace. (b)The gold film grating has a 600 nm periodicity with 30 nm depth modulation and 50% duty cycle as measured by AFM.

coupling angle for the corresponding wavelength, the image in reflection shows significant attenuation of light in regions of SPP resonance coupling as compared to images at non-resonant angles; refractive index changes in the dielectric support that shift the coupling angle are measured as intensity shifts. This technique known as surface plasmon resonance imaging is routinely employed for the readout of immunoassays in biosensing in which highly multiplexed sites for binding kinetics must be rapidly observed in parallel [WO14].

Towards SPR resonance imaging, individual sensing sites as a pixelation of the SPP resonant grating sensor were developed. Formatted as pixelated elements, lateral design of the patterning provides control over heat capacity and conductance to maximize the signal for individual resolution elements, as well as providing control over the minimization of thermal-cross talk between pixels. As the SPP resonant grating coupler requires subwavelength resolution in fabrication as well as the available throughput to pattern in an array format, it is desirable

to employ a fabrication process that allows for large scale patterning with high resolution. A candidate for these criteria is nanoimprint lithography, where a high resolution mold of the desired negative pattern is impressed upon a thermo- or photo- curable plastic film, which can be removed upon curing to contain the designed pattern. When the resist is hosted by a wafer substrate, traditional liftoff and etch steps can be subsequently performed upon the imprinted pattern, allowing for the transfer of the pattern into the substrate itself. This technique achieves resolution scales comparable to electron-beam lithography, and can repeatedly transfer patterns from an electron-beam resolution mold to entire wafers, amenable for rapid large scale patterning.

A nanoimprint process was developed for the thermal-IR SPP resonant sensor pixels. The substrate used was prime grade borosilicate glass; the choice of glass lowers the substrate conductivity as compared to silicon substrates, an advantage to be claimed by forgoing electrical ROIC. The substrate, with roughness < 5 nm across the substrate, was solvent cleaned and a sequential 5 nm Ti adhesion layer and 200 nm Au film was evaporated by electron-beam evaporation onto the substrate for the eventual patterning of the supporting gold gratings (Temescal BJD 1800). The substrate was then spin coated with 75 nm of PMMA, with 90 sec soft bake at 180^o C, and 160 nm of AR-UVP imprint resist (Fig. 3.3a-1). An electron-beam patterned master mold with a 500 x 500 μm^2 area of a one-dimensional SiO2 grating with 1 μm depth and 600 nm periodicity with 50% duty cycle was fabricated, and transferred to a secondary polymeric stamp for imprinting into the imprint resist. The stamp was imprinted into the resist by hard contact through nanoimprint lithography tooling (EVG aligner), and subsequently reactive ion etched (RIE) using CF_4 and oxygen gases for respective top layer residue etch and PMMA under layer etch, with the top layer acting as a polymeric mask (Oxford RIE P80) (Fig. 3.3(a)-2). Following this step, 30 nm of Cr was deposited by electron beam metal evaporation, and immersion in acetone for liftoff was performed (Fig. 3.3(a)-3). With the Cr pattern as an etch mask, RIE etch was directly performed into the gold using a CHF_3 gas. Finally, the Cr etch mask was removed by Cr etchant, which was measured to be highly selective against Au and its adhesion layer, owing

to the conformality of the Au film. Etch modulation depth of 30 nm into the gold and periodicity of 600 nm with 50% duty cycle was verified by AFM measurements (Fig. 3.3(b)).

Since the detector sensitivity is dependent on the magnitude of refractive index shift in the dielectric per unit temperature shift generated by thermal infrared absorption, a higher thermo-optic coefficient (TOC) was desired for the IR absorption dielectric layer (Fig. 3.3). Polymers have been reported for high coefficients of linear thermal expansion compared to glassy materials, and possess comparably higher thermo-optic shifts [ZZLS06]. Parylene-C is a polymer known for its mechanical, thermal and chemical stability, used often as a protective coating for anti-fouling and biocompatibility applications with excellent longevity [ZZLS06, SCL^{+}03]. Such material is desirable as a dielectric layer that can repeatedly transduce small temperature changes through IR absorption without suffering lifetime drift in the base refractive index or sensitivity degradation by hardening. With the reported linear coefficient of thermal expansion to be 3.5 x 10^{-5} K^{-1}, an empirical formula was used to calculate the TOC for parylene-C to be -6.3 x 10^{-5} [ZZLS06], about 2.5 higher than reported measurements of silicon nitride thermo-optic coefficient of 2.5 x 10^{-5} RIU$^{o}C^{-1}$ [AG13]. Fig. 3.4 shows the Fourier transform infrared (FTIR) spectroscopy analysis of parylene-C with absorption bands in the 7-14 μm region conducive to transduce the absorption of thermal IR light to thermo-optic shifts measurable by SPP resonance. Having characterized the IR absorptivity of parylene-C in the band of interest, a parylene coater system (SDS PDS2010) at 15 mTorr chamber pressure was used to vaporize 1g of parylene-C dimer at 50^{o} C, converted into monomer by pyrolysis at 550^{o} C and polymerized onto the fabricated SPR grating-pixel for a conformal 530 nm parylene-C thin film (Fig. 3.3(a) step 4).

To measure the imprinted IR sensitive SPP resonant pixels developed by SPR imaging, a quasi-monochromatic collimated LED source centered at 780 nm illuminates the grating at a fixed angle of 24^{o} with respect to the sensor surface normal, and is polarized in the plane of incidence as a transverse magnetic (TM) wave (Fig. 3.5(a)). While the resonance angle can be calculated to be at 26.5^{o}, the implemented angle is slightly offset in order to maximize the shift contrast

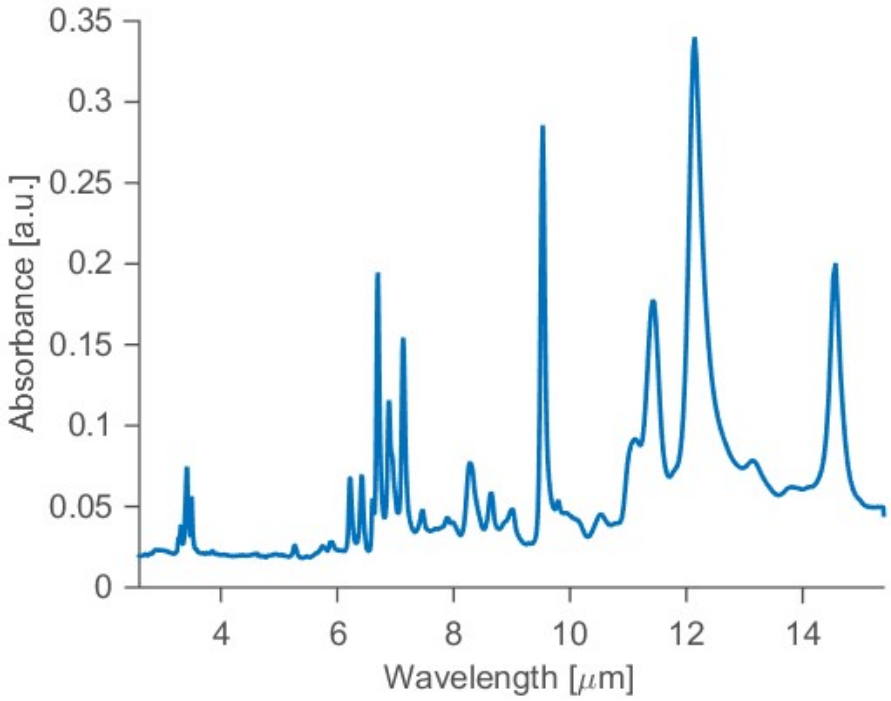

Figure 3.4: Fourier transform infrared (FTIR) spectroscopy of Parylene-C is conducted in attenuated total internal reflection (ATR) mode. Strong absorption bands can be seen in the 8-14 μm spectral band, amenable for thermal infrared detection. In conjunction with a high thermo-optic coefficient, and intrinsic thermal stability, the thermal band absorptivity of parylene-C functions as the IR sensitive layer for SPR imaging. Strong bands also exist in the extended 6-8 μm region, allowing for higher temperature sources centered in this region to maintain high signal contrast with limited saturation effects.

dynamic range (i.e. biased at the maximum lineshape slope). In reflection, a CMOS camera (eCon See3Cam 12CU-NIR) and f = 7.5 cm optic images the grating pixel. For the thermal source, a separate arm is angled at approximately 45^o and a 7-12 μm anti-reflection coated Ge filter is placed to block out Si detector sensitive bands in the visible spectrum below 1.975 μm emitted from the thermal source that might contaminate the sensor signal, and provide a window for the 8-14 μm thermal IR band. The thermal source is imaged from infinity onto the pixel by an f/2 ZnSe optic.

Two heating elements were used as thermal sources: in addition to the nitride igniter previously described at approximately 1600 K, a soldering iron measured by thermocouple to be 423 K was also imaged. While optically shuttered, the sources are allowed to reach thermal equilibrium as the optical readout system obtains a baseline to acquire the sensor noise figure σ, the standard deviation. With a sufficient 1 min baseline at 20 fps averaged to 0.33 Hz sample acquisition, the shutter is opened and the measured intensity responses are well fit to a first order differential equation time response. Shown in Fig. 3.5(b), the signal response is normalized to the 3σ according to the obtained baseline, termed 1 response unit (RU); the sensor measures the igniter response to be approximately 26 RU, and the solder iron response is measured to be approximately 3 RU. The fit extrapolated rise time constant is 31 s, with similar agreement for the fall time.

A plot showing the additional increase in thermal radiance of an object over 293 K emitting in the 8-14 μm band is shown in Fig. 3.6, and the measured thermal sources are plot-ted according to a unity emissivity. Since non-unity emissivities emit lower spectral radiance, the band radiance from an ideal blackbody at the same temperature is greater than or equivalent to the non-ideal radiance. Thus, the calculation based on ideal emissivity presents an upper bound on the radiance emitted by an object at the same temperature, and transitively, an upper bound on the noise equivalent temperature difference (NETD). The NETD is the temperature difference between an object and the background necessary to induce a variation in the detector equals to

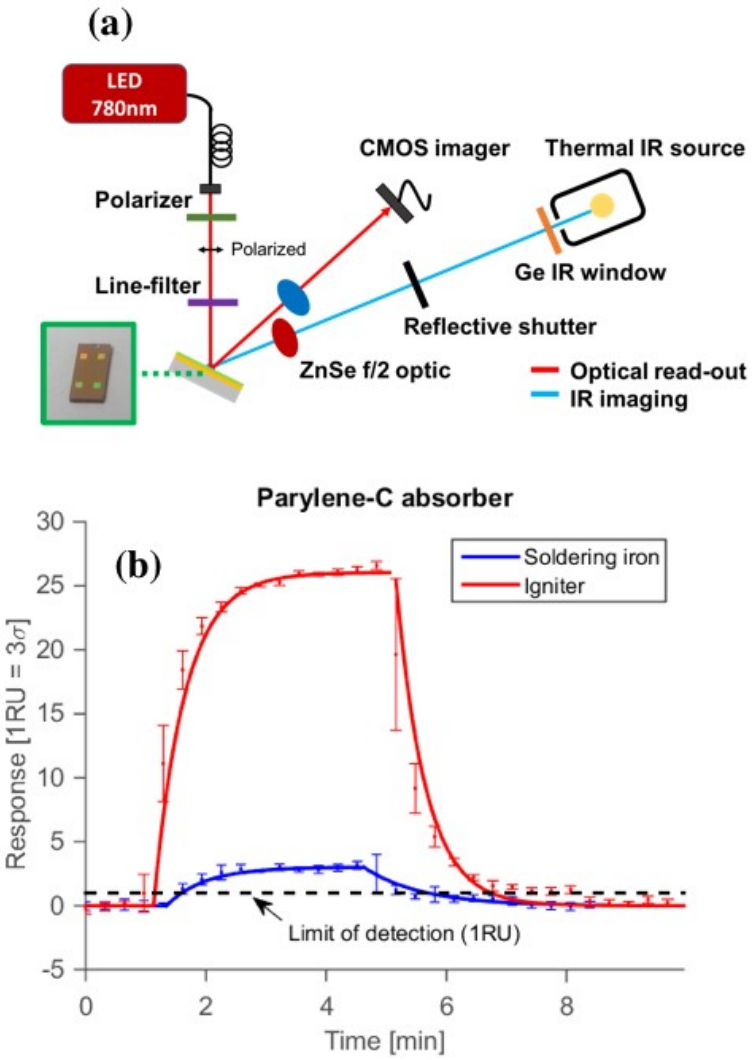

Figure 3.5: Measurement setup for SPP resonance imaging detection of a thermal source (a) consists of an infrared imaging path (blue) and a visible readout path (red), with the two paths coincident on the polymeric grating sensor (green). The absorption by a single 500 x 500 μm^2 SPP resonant pixel is measured (b) in real time and any background fluctuations of the source are removed by a non-resonant control region. Intensity units are normalized by the measured baseline noise power σ to response units such that 1 RU = 3σ. A soldering iron at 423 K and a nitride igniter at 1600 K are measured.

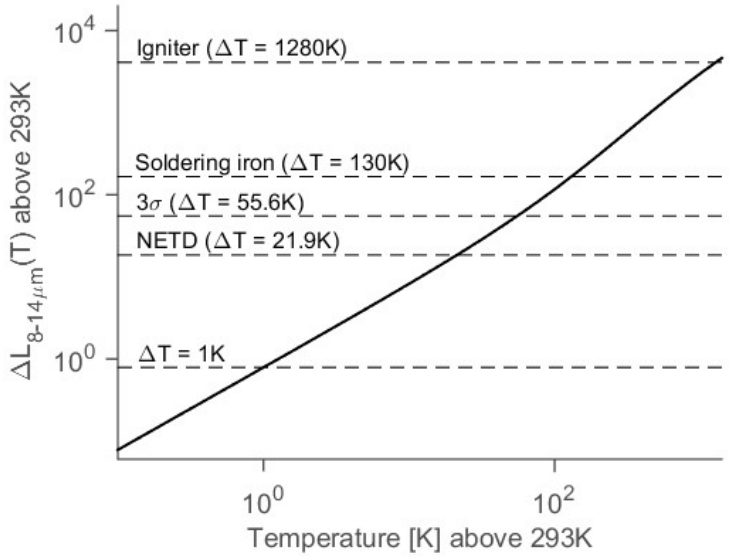

Figure 3.6: For ideal radiators above room temperature, the net band radiance difference in the 8-14 μm band over a 293 K blackbody is calculated from the Planck law spectral distribution. The differential radiance for the thermal sources measured are charted, and based on the detected thermal signal from the T = 423 K soldering iron source, the noise equivalent temperature difference could be calculated as 21.9 K, the object temperature with the proportional spectral radiance to induce a measured noise equivalent to 0.33 RU (or σ) signal response.

its noise, i.e. 1σ In our device, the temperature difference in the imaged source compared to its back-ground required to induce a 0.33 RU sensor response can be extrapolated to be NETD = 21.9 K.

Improvements upon the time constant are desirable, and the effects of lateral thermal isolation for the pixel on the sensor heat capacity was investigated. To implement this isolation, approximately 0.5 μm wide and 1 μm deep trenches were milled by focused Ga ion beam along the 500 x 500 μm perimeter of the pixel (FEI Scios Dual-Beam), as shown in Fig. 3.7(a). Imaging the nitride igniter up-on this modified sample, the characteristic time constant was shown to decrease by a factor of 2 upon the pixel delimitation (Fig. 3.7(b)). By setting delimitations, the heat capacity was restricted to the delimited pixel area in addition to a restriction on the lateral heat conductance to non-resonant areas outside the grating pixel dimensions, leading to a slight rise in the signal response and a larger decrease in the device time response. Similar to

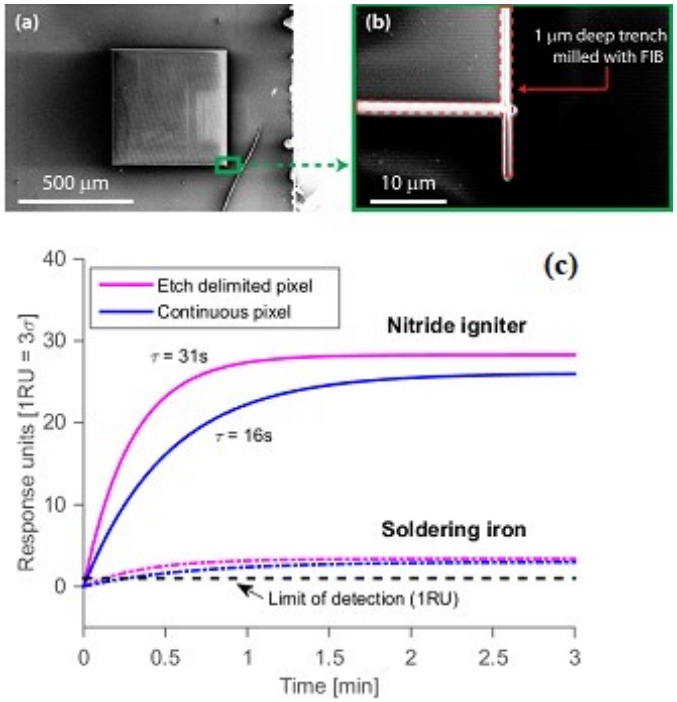

Figure 3.7: Focused ion beam etching about the perimeter of the 500 x 500 μm^2 thermal IR SPP resonant grating pixel (a) limits lateral heat conductance from the heated pixel; etched trenches are marked in red. For an approximately 1 μm etch depth by FIB milling (b), a characteristic time response of 16 s was observed for the limit of detection and a 1.93 factor decrease in the characteristic time response was observed (c).

isolation techniques employed in bolometer design, simple etch steps incorporated into grating pixel fabrication for the thermal-IR SPR sensor can serve to control and improve the detector time response and SNR. This demonstration shows that the response time can be dramatically improved with careful consideration to the pixel size, and delimitation towards thermal isolation.

3.3 Conclusion

A thermal infrared detection platform based on SPR imaging was fabricated and measured. Nanoimprint lithogra-phy was used to generate SPP resonant sensor elements in pixel format and parylene was demonstrated in its capacity as a thermo-optic polymer. An inexpensive CMOS imager and LED were employed to acquire readout of the thermal shift by SPR imaging. Through

this system, characteristic sensitivity and response times of the SPR thermal imaging sensor were experimentally characterized and delimitation of the pixel was shown to be a design element capable of improving response time.

This chapter is in full, a reprint from a manuscript published in Applied Material and Interfaces, 2017, Hong, Brandon; Vallini, Felipe; Fang, Cheng-Yi; Alasaad, Amr; Fainman, Yeshaiahu. The dissertation author was the primary author of this manuscript and Yeshaiahu Fainman was the principal investigator.

Chapter 4

Channel Dispersed Fourier Transform Spectrometer

4.1 Introduction

A significant limitation to obtaining spectra by stationary interferometery is the inability to achieve high resolution spectra. While increasing the optical path delay within the detector array is possible, the fixed pixel size leads to a decrease in the sampling rate with increasing fringe density. Spectrometers with significant pixel density [IKH16] have been developed, however, the interferogram is inherently one dimensional, and is thus limited by pixel density in a single dimension, with the pixels along the opposing dimension presenting a redundancy.

To improve the spectral resolution of stationary FT spectrometers, we introduce a channel dispersed Fourier transform (CDFT) spectrometer that records two-dimensional spatial interferograms using imaging detectors in a single-frame snapshot to recover high resolution spectra. By spectrally dispersing the one-dimensional interference pattern, an array of bandlimited interferograms is measured in real time, relaxing sampling constraints within each spectral channel. Bandlimited channels also reduce centerburst contrast, lowering the quantiza-

tion noise set by detector dynamic range. To demonstrate the CDFT spectrometer, broadband spectral domain optical coherence and multi-color quantum dot photoluminescence are measured using low pixel-density detectors. Through efficient use of the full pixel count in imaging detectors, the resolution improvement of CDFT spectrometers offers a route to a compact and precise in situ spectrometer, useful for environmental management, medicine, and security [IKH16, ZBC$^+$14, Fan14, RDC17, RSA11, ZIM$^+$13, MLL14].

4.1.1 Principle of Operation

The CDFT spectrometer can be understood as an extension of the well developed stationary Fourier transform spectrometer. For stationary Fourier transform spectrometers, the 1D interferogram spans a detector column by path delay, and for a zero path delay (or center burst) at the column center, the total path difference is inversely proportional to the minimum resolvable spectral element. Sampling rate is determined by the optical path difference equal to pixel pitch, or equivalently, the number of detector pixels sampling the interferogram. For spectrum signal bandwidth of K_B and desired resolution Δk of the following equation is valid:

$$N_{px} > \frac{K_B}{\Delta k}$$

where N_{px} is the number of pixels along the interferogram direction. Hence, for a fixed signal resolution, decreasing signal bandwidths results in a stationary Fourier transform spectrometer with lower pixel density in fixed-size detector arrays in order to recover the spectrum without aliasing.

The CDFT spectrometer design optically disperses the one-dimensional interferogram pattern across a two-dimensional detector array. The spectral dispersion can be generated by prism, diffractive element, or any similar dispersive spectral mapping component. With the spatial interference pattern oriented along the detector columns, the pattern image is dispersed

perpendicularly in horizontal direction and resolved along the rows of the detector array. In this two-dimensional interference pattern, each column interference pattern, or "spectral channel" is formed by a sub-band of the signal spectrum and can be Fourier transformed to recover the sub-band spectrum [VSW91]. After processing for carrier frequency aliasing and background, the recovered sub-band spectra can be added to recover the full signal power spectrum. While each spectral channel can be of a single-pixel width, channels with multi-pixel widths can be binned to a column with single pixel width. Once the spectral channels are defined, the band limits are determined by both the dispersion angle subtended by the column extent. For a total signal bandwidth spread evenly across N_{py} spectral channels, the tradeoff can be described as follows:

$$N_{px} > \frac{K_{B,channel}}{\Delta k} = \frac{K_B}{\Delta k N_{py}} \iff N_{px} N_{py} > \frac{K_B}{\Delta k}$$

Since each spectral channel bandwidth now occupies a smaller fraction of the total signal bandwidth, the minimum number of pixels along the interference axis needed to avoid aliasing is now lowered by the number of channel divisions N_{py}.

For comparison, we consider a long-wave infrared (LWIR) spectrum measured from 1450 to 650 cm^{-1} (roughly 7-15 μm, matching the responsivity of an uncooled infrared focal plane array). For a stationary Fourier transform spectrometer that uses a linear array with 640 pixels, the highest generally achievable resolution without aliasing is 1.3 cm^{-1}, or 13 nm for spectral features near 10 μm. Because the sampling rate is fixed by the pixel count of the detector array, increasing the interferogram window also results in reduced sampling rates, towards the Nyquist limit. In contrast, for a CDFT spectrometer, a large-format focal plane array with 640 by 512 pixel dimensions can recover spectra with 0.0025 cm^{-1} resolution or 0.025 nm for spectral features near 10 μm. Through spectral dispersion, the bandwidth per channel is reduced by the number of channels partitioning the total signal bandwidth; the minimum sampling rate of the interference pattern in each channel is reduced by the number of pixels (or channels) in the introduced detector

axis, and the interferogram window can be increased proportionally to maximize the spectral resolution.

In practice, it is critical that the shearing angle of the interference pattern is chosen such that the channel bandwidth is not itself aliased [VSW91]. In particular this is the condition that an integer multiple of the sampling rate does not directly fall into the channel band, this condition can be met by translational alignment of the detector along the dispersion axis, or by fine tuning of the shearing angle to move the sampling rate to a channel band edge. Moreover, the system optical transfer function lower bounds the minimum resolvable linewidth. While the interior angle of the interference waves can be increased within the bandpass sampling limit, system apertures will restrict the visibility of higher spatial frequency components of the FT interferometric pattern, and lower the SNR of high frequency components in the recovered spectra. Moreover, wideband system noise (both shot and detector) is itself aliased in bandpass sampling, and noise is introduced into the signal band with decreasing sampling rates to further lower the SNR. Judicial design of the optical system and selection of its elements is necessary to compensate for higher order errors. Simulations illustrate advantage of CDFTS in avoiding undersampling corruption and the reduction of signal dynamic range.

4.2 Experiment

4.2.1 Optical setup

The CDFT spectrometer is an extension of the Sagnac interferometer. As described in Fig. 4.1(c), the signal beam is split by a 50:50 beam-splitter reflected across the same three mirrors forming the ring, in opposite circuits to create two beam paths; adjustable in-plane tilt in the central mirror creates angularly displaces the two paths for an interference pattern. A lens (L1) is then used to form an intermediate spatial Fourier (SF) transform plane, allowing for separation of the two beams for spatial filtering and background calibration. Prior to dispersion, a periscope

assembly is used to rotate the interference plane by 90^o out of the table plane; this allows the now out-of-plane interference pattern to be dispersed in the table-plane along the detector. Similar system topologies are employed in pulse characterization system [Tre11, PPF05], where in CDFT spectrometers, the aim is to distribute the spectral information across all detectors in an imaging detector and maximize spectral resolution (see Fig, 1(b)). The dispersive element is a Pelin-Broca prism (Thorlabs) for 90^o dispersion, and the spectrally dispersed interference pattern is resolved by a cylindrical mirror with curvature in the dispersion plane onto the CMOS imager (Point Grey Blackfly, 2.3 MP monochrome).

The experimental implementation of CDFT spectrometer is shown in Fig. 4.1(c). An interferometric arm based on a Sagnac interferometer splits a collimated signal beam into two beams with an interior interference angle proportional to the tuning mirror tilt; this topology has been thoroughly studied as an interferometer and stationary Fourier transform spectrometer [Bar85]. The typical stationary Fourier transform spectrometers interference pattern is shown schematically in Fig. 4.1(a). Based on the interior angle, control of the tuning mirror tilt allows for variable shearing of the counter-propagating beams in the Sagnac ring and thus fringe density in the final interferogram. A prism is used to spectrally disperse the broadband spatial interference pattern into a spread array of bandlimited interference patterns, and is resolved by an imaging camera. Recorded interferograms are then binned into spectral channels, and 1D Fourier transforms of the channel interferograms are computed by fast Fourier transform (FFT) in MATLAB; high pass filters are applied to each channel interferogram to remove out-of-band baseline noise spectra while preserving in-band channel components. For low sampling rates, aliased spectral channels are unwrapped from un-aliased components into an empty half space and summed to reconstruct the complex spectrum; recovery of the power spectrum is obtained from the spectral magnitude. A CDFT spectrometer was constructed according to the previously described schematic to measure the spectrum of modulated xenon arc lamp emission. Since the advantage of CDFT spectrometers is in measuring broadband spectra with narrow spectral

features, we use this technique to evaluate the spectrum of a broadband xenon arc lamp output from a Michelson interferometer. Increasing displacement of the delay mirror from the point of zero optical path difference introduces a sinusoidal modulation of the optical spectrum with increasing spectral fringe density. This technique is the basis for depth imaging in spectral domain optical coherence tomography, and for spectral evaluation, is useful for generating arbitrarily dense spectral features over a broad signal bandwidth. In this experiment, the broadband signal is used to demonstrate the effect of aliasing in undersampled interferograms of stationary Fourier transform spectrometers, and how channel dispersion in CDFT spectrometers can recover and restore the narrow spectral features.

4.2.2 Results

The modulated xenon spectrum was passed through the CDFT spectrometer as described in Fig. 4.1, and was recorded as a 2D interferogram by the CMOS imager with 1900 x 1200 pixel format (row, column); the interference pattern runs along the columns. To demonstrate the efficacy of the system as a low pixel-density stationary interferometer, two binned formats are processed, with 128 x 1200 (row, column) and 128 x 256, corresponding to un-aliased and aliased spectra, respectively. In Fig. 4.2, experimental recovery for 128 x 1200 format is shown. The raw interferogram for the 128 x 1200 format is obtained (Fig. 4.2(a)), and the spectral channel interferograms in each column (Fig. 4.2(b)) are first zero-padded for interpolation in the spectral domain and then individually Fourier transformed by FFT. The recovered normalized magnitudes of the channel spectra are shown in Fig. 4.2(c); with increasing channel number, the center wavelength is shown to increase, corresponding to the spectral dispersion in the CDFT interferogram. Moreover, the dispersion also partitions the total spectrum between the pixel columns, and the recovered channel spectra can be seen to be localized to a narrow-band about their center frequency. Owing to the linearity of the center frequency dispersion, it is evident that the signal is not aliased owing to the sufficient sampling of the interferometric axis by 1200

pixels, and recovery of the full spectrum is achieved by computing the magnitude in sum (Fig. 4.2(d)).

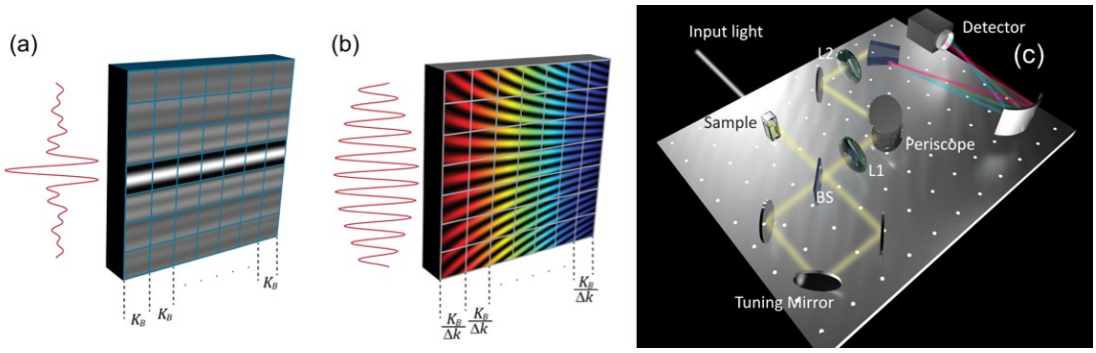

Figure 4.1: A stationary Fourier transform spectrometer measures the spatial interference pattern of a signal in a single dimension (a) and obtains the spectrum by Fourier transformation. Spectral dispersion in a CDFT spectrometer (b) creates an array of narrowband interferograms in the detector columns that partition the signal spectrum. Schematic diagram of a CDFT spectrometer (c) where spatial interference is generated by Sagnac interferometric arm; interference angle is determined by tuning mirror tilt. Periscope assembly rotates the interference plane by 90^o to allow for dispersion in the propagation plane. Dispersive arm spreads the signal interference pattern into sub-band spectral channels to form the CDFT interferogram and is recorded by a 2D imager (Detector).

Because of the sufficient density of pixels along the interferometric axis (1200 pixels), recovery in this case does not provide a sampling advantage over the 1D stationary Fourier transform spectrometer, as the interferogram is oversampled for all channels. Since there is no aliasing between the spectral channels or spectral overlap, the summation of recovered channel spectra is equivalent to the summation or binning of channel interferograms into a single 1200 x 1 array. In this case, alias-free recovery is enabled by the high density of pixels along the interferometric vertical axis of the detector.

The CDFT sampling advantage is evident in low pixel density detectors where undersampling occurs. This sampling advantage can be shown in the experimental recovery of a 128 x 256 (row, column) format CDFT interferogram, where using a 1D stationary spectrometer of the longest pixel dimension is insufficient to sample the entire 500 nm bandwidth of the visible band while retaining the single nanometer features. At the same shearing angle as before for

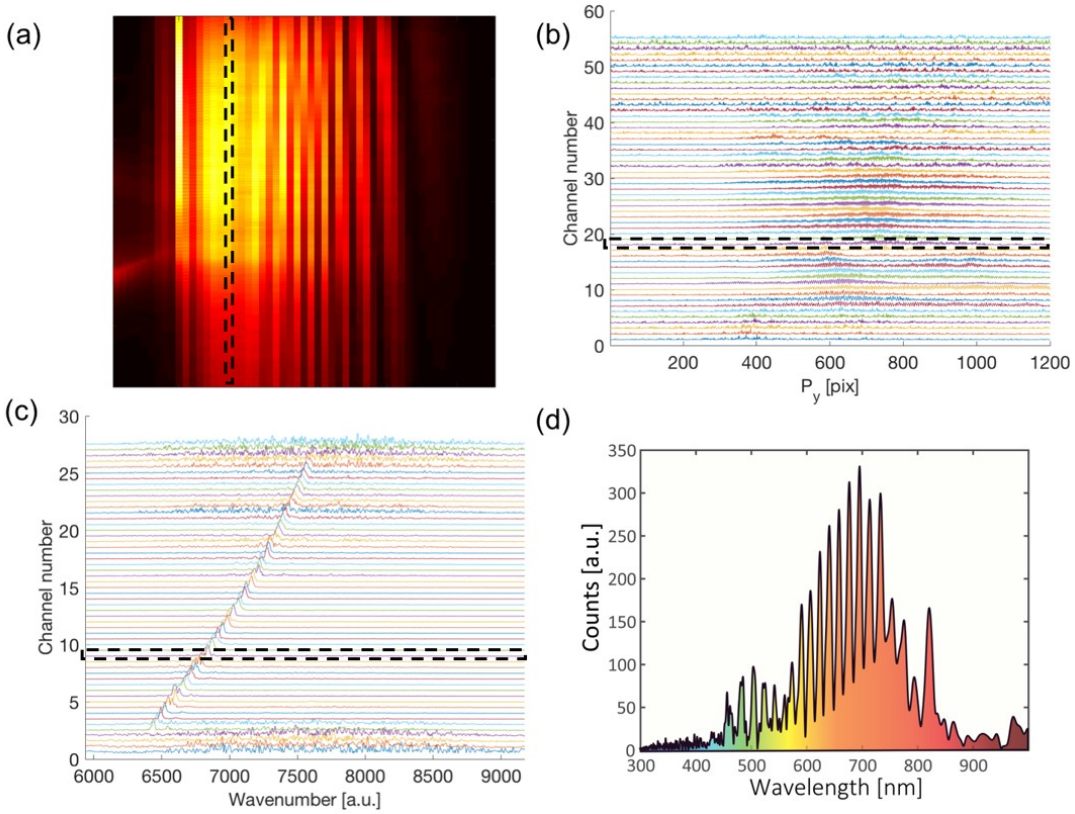

Figure 4.2: Expeirmental 1200 x 128 pixel (column, row) CDFT interferogram of a broadband Xe lamp spectrum modulated by a Michelson interferometer to generate narrow spectral lines (a) with dispersion channels across the columns and interference along the rows. Each column contains a sampled interferogram (b) that is band-limited by the dispersion across the column width. Fourier transform of each channel results in the recovery of a sub-band of the total spectrum, and the normalized magnitudes are shown in (c). Without aliasing, evidenced by the linear dispersion of the channel center frequencies, summation of the complex channel Fourier transforms yields the recovered signal spectrum.

identical spectral resolution, the binning of the native detector format brought the signal to a 128 x 256 format is obtained with each column as a spectral channel sampling the interference pattern with 256 detectors. After zero-padding interpolation as before, the channel spectra are recovered by FFT and shown in magnitude in Fig. 4.3(a): here, the low-density of pixels shows aliasing to occur for small signal wavelengths. As a result of undersampling, simple summation (Fig. 4.3(c)) of the channel spectra results in an aliased signal spectrum, identical to 1D stationary Fourier transform spectrometer signal recovery. Since the channel center-frequencies are linearly

dispersed, the wrapping or ”reflecting” of the dispersion back into the sampling bandwidth is symptomatic of aliasing and cannot generally be distinguished for dense spectra in the 1D case. Owing to the channel separation in CDFT interferograms, these wrapped spectral channels can be uniquely separated from overlapping channels, and unwrapped or reflected across the Nyquist frequency into an empty half-space as in Fig. 4.3(b). Following this processing, the channel summation of recovered sub-bands can be repeated, and the alias-free CDFT recovery of the total spectrum is shown in Fig. 4.3(d).

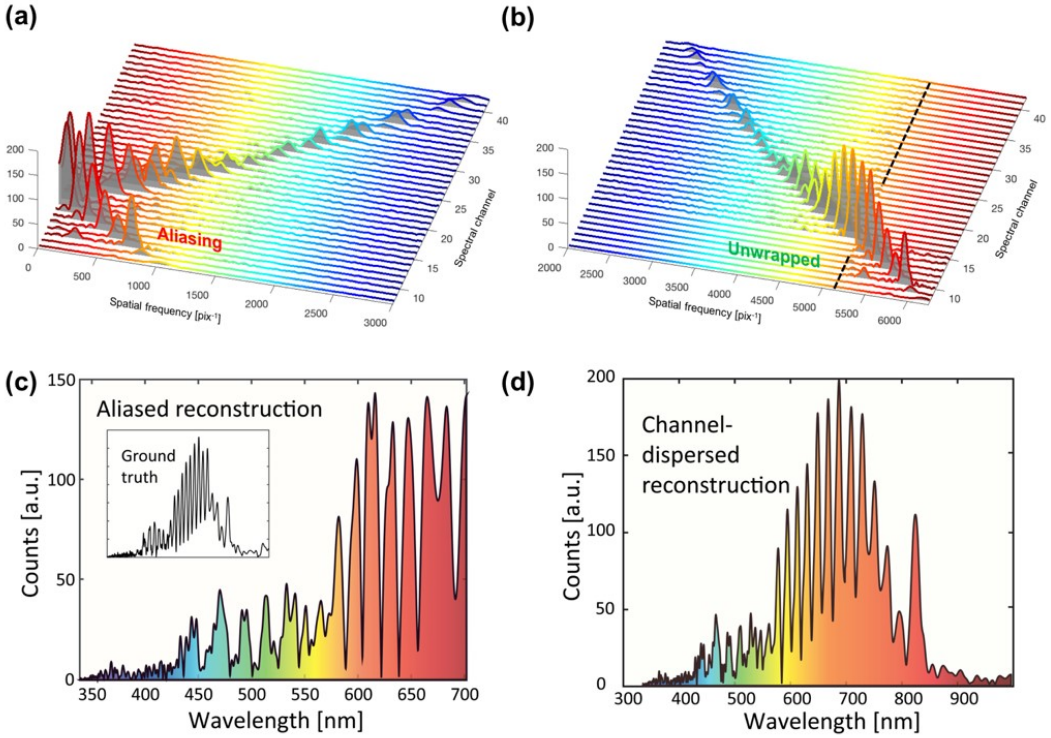

Figure 4.3: Experimental 256 x 128 pixel (column, row) CDFT interferogram of spectrally modulated Xe lamp. The Fourier transform recovered channel spectra magnitudes (a) show wrapping of the linear dispersion about the Nyquist zone for short wavelengths, indicative of undersampling and aliasing in these channels. When simply added, irreversible aliasing is observed in the magnitude (c) as shorter wavelengths are reflected across the critical sampling frequency to overlap with longer wavelengths; this is equivalent to the spectrum recovered from the 1D interferogram of a stationary Fourier transform spectrometer. CDFT spectrometers allow the separation of the aliased components from overlapping channel spectra. Linear dispersion of the spectral channels is restored by unwrapping the aliased channels into an empty half-space (b) and recovery by summation recovery (d).

To test the applicability of low pixel density CDFT interferograms, multicolor quantum dot fluorescence measurements over a broad spectral range were measured. With the increasing sophistication of both laboratory and consumer imaging systems, multicolor/channel detection of fluorescent tags is an important direction towards high throughput analysis in immunoassay and biological sensing as a whole. A simple side collection fluorescence measurement was performed in a 1 mm path length glass cell, and a 400 mW Ar-ion laser was used to excite QD luminescence. Solutions of 6 nm diameter CdSe/ZnS quantum dots (1 mM in toluene) were individually measured for PL in both high (128 x 1200) and low (128 x 64) pixel density environments by camera binning. A final measurement of a quantum dot mixture (300 μM) was performed in both pixel-density environments, and processed spectra of individual QDs and mixture are shown in Fig. 4.4. Spectral dispersion was maintained along the constant 128 pixel axis, while interferogram sampling was variable between high and low pixel-density environments. In the high pixel-density imager, alias-free spectra are obtained, as the sampling of the interferogram is well within the Nyquist rate (Fig. 4.4(c)). In the case of the low-pixel density environments, the spectral channels can be observed to overlap (Fig. 4.4(a)) and the equivalent 1D interferogram is shown to recover an aliased signal spectrum (Fig. 4.4(d)). Using the unwrapping routine allowed by CDFT spectrometers, the overlapped spectral channels can be flipped into the empty spectral-half space and superimposed to recover the unwrapped spectra (Fig. 4.4(e)).

4.3 Discussion

In our derivation, it was shown that by dispersion, the total signal bandwidth in a single interferogram can be divided into sub-bands that can sample the interferogram at a lower rate without aliasing. In particular, for a given number of pixels N_{py} along the interferometric axis, the critical Nyquist sampling rate can be lowered by a factor of N_{px}, the number of dispersion

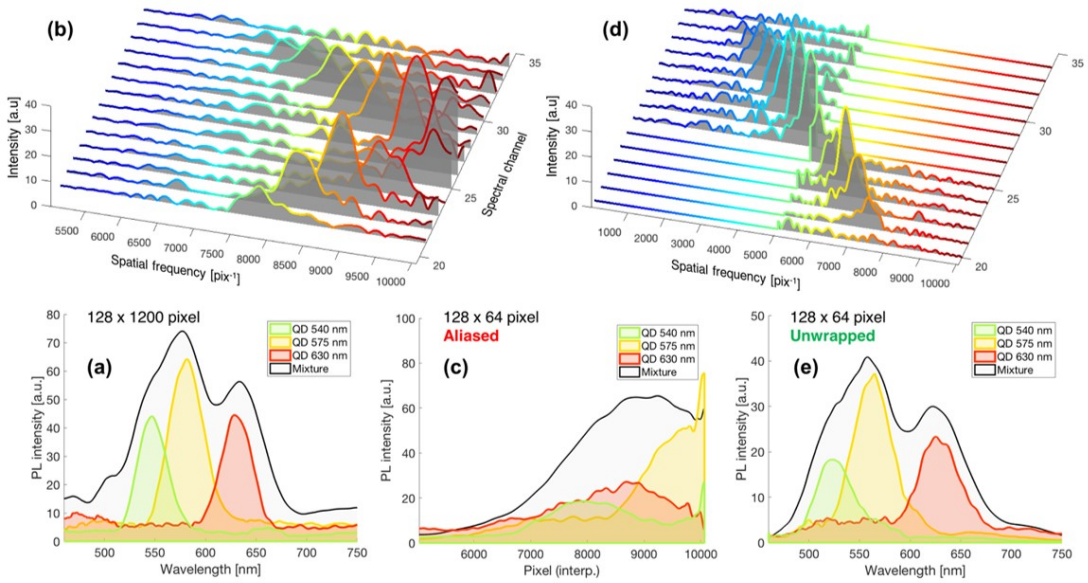

Figure 4.4: CDFT spectral measurements of CdZnSe quantum dot luminescence spectra. In a high pixel density configuration (a), 128 binned spectral channels with 1200 pixel path delay sampling each are used to measure and recover monodisperse quantum dot PL (colored curves) at λ_{em}=540, 575, and 630 nm. A mixture of the quantum dots is measured to recover broadband PL (gray). In a low pixel density configuration, the 128 spectral channels are further binned to a 64 pixel sampling. As the carrier Nyquist rate is undersampled, spectral wrapping in the channel magnitudes is observed (b) resulting in an aliased spectrum recovery (c). CDFT spectrometer separation of the channel spectra in measurement allows for unwrapping of the overlapped bands (d) to reconstruct the alias-free signal spectrum (e).

channels. This allows the detector to measure proportionally larger path delays to allow for a resolution increase by a factor of N_{px}. While the carrier frequency, or channel center frequency is more readily aliased as a value invariant with the number of spectral channels, knowing the dispersion center in each channel allows the recovered spectra to be uniquely unwrapped from about the Nyquist edges and restored without aliasing; this was demonstrated in our experiment for aliasing across a single Nyquist edge. For highly undersampled interferograms, aliasing can potentially occur across both Nyquist edges, and more rigorous methods for spectral unwrapping will be necessary. To calibrate this process, known broadband spectra with dense features such as the spectrally modulated Xe lamp used in our experiment can be used to determine the number of wraps across Nyquist edges by tracking the channel spectra with increasing interference angle.

In particular, the center frequency for each sub-band can be followed in each channel as the interference angle increases, and at the target angle for the desired spectral resolution, the center frequency of each sub-band will determine the number of reflections to make across each Nyquist edge.

4.4 Conclusion

We have demonstrated a channel dispersed Fourier transform spectrometer and have shown that spectral dispersion of the 1D stationary Fourier transform interferogram allows for the interferogram to be undersampled in proportion to the number of spectral channels introduced. CDFT spectral evaluation allows for high spectral resolution to be achieved for stationary infrared Fourier transform spectrometers in a format native to sensitive low pixel density imagers that populate much of the mid-IR and far-IR range. Conversely, with the reduced dependence on linear pixel density, high pixel density imagers in the visible and NIR can be partitioned for hyperspectral imaging by integration with a compact implementation of parallel CDFT spatial filters. Moreover, high speed cameras that scan rapidly over a limited number of detector elements can also benefit from channel dispersion, and in applications such as optical coherence tomography, CDFT spectrometers can improve the speed of A-scan readouts in the spectral domain without sacrificing dynamic range or resolution.

This chapter is in full, a reprint from a manuscript published in Nature Communications Physics, 2018, Hong, Brandon; Monifi, Faraz; Fainman, Yeshaiahu. The dissertation author was the primary author of this manuscript and Yeshaiahu Fainman was the principal investigator.

Chapter 5

Surface Plasmon Resonance Profilometry and Dynamic Optical Patterning of Thin Liquid Dielectric Films

5.1 Introduction

Determining the topography of thin liquid dielectic films (TLDFs) is of a fundamental importance for the basic studies of interfacial science such as wettability and spreading [Bon09, OKM09], response to external stimuli in both physical [ODB97] and bio systems [Gro01], and in numerous industrial applications such as coatings, insulating layers and surface modifiers [YRKF94, SAO05]. While one of the commonly used methods to determine the thickness of TLDFs is white light interferometry, the sensitivity of this method to local small thickness variations is low, especially when the film thickness is lower than the optical wavelength due to the low reflection from the film's surface.

One attractive possibility to enhance this sensitivity is to utilize a Surface Plasmon Polariton (SPP) illumination which takes advantage of the resonant oscillation of conduction

electrons at the interface between metals and dielectrics [Pin55, Rit57], which supports SPPs - electromagnetic waves that propagate along the metal-dielectric interface and strongly decay in the direction perpendicular to it [H.R13, Mai07].

This localization property makes SPPs very sensitive to the dielectric properties of materials in close proximity to the metal surface, which over the last few decades led to a wide spectrum of sensing and imaging techniques such as surface plasmon spectroscopy and surface-plasmon resonance microscopy (SPRM) [WK88, HWKS89, FKP^{+}95]. In particular, SPRM is a well established method for label-free imaging of low contrast features such as roughness of thin dielectric films [SWKa95], small bio-objects such as bacteria, virus particles, biofilms as well as detection of analytes as a result of surface reactions. The latter typically result in an assembly of a monolayer array of molecules of a few nm thickness bound to metal surfaces, which modifies SPP momentum (e.g. by changing the refractive index), and found numerous applications in biosensing [Lof91, Yea96, Hom06, GK07].

In this work we experimentally determine TLDF's topography of with features of thickness comparable or smaller than the penetration depth of an SPP into the direction normal to the metal surface, typically of the order of magnitude of the corresponding wavelength in the free space. Fig.5.1(a) presents key elements of our system under study; metal grating of period Λ and an adjacent layer of TLDF of thickness w as measured from bottom part of the grating grooves. Our method relies on capturing angular and spatial content of the beam reflected from the sample, referred below as $k-$space and real-space imaging, respectively, which correspond to illumination configurations of an incoming TM-polarized light of a fixed wavelength described in Fig.5.1(b) and Fig.5.1(c).

$K-$space imaging utilizes a focused Gaussian beam (Fig.5.1(b)) and a collimated beam at the back focal plane (BFP) presented at Fig.5.1(d), whereas the real-space imaging utilizes a dual configuration with an incident plane wave of a given incidence angle (Fig.5.1(c)) which corresponds to a focused beam at the BFP, described in Fig.5.1(g). Fig.5.1(e,f) shows representative

imaging results of the BFP with inward and outward pointing dark arcs separated by a distance D along the central line (see also [JH14] for k-space imaging of metal gratings covered with solid dielectric).

Importantly, D together with the inward or outward pointing configuration of the dark arcs, sets uniquely the absorption angle and the corresponding TLDF's thickness at the illumination spot. The emergent patterns are related to the Kikuchi patterns or Kossel lines [KLa35] that have been observed in atomic structures through electron microscopy and Brillouin zone spectroscopy of photonic crystals [Bar05]. In the real-space imaging (Fig.5.1(c,g)), the reflected light due to a plane wave incident beam is indicative of spatial regions where resonant coupling condition holds. Fig.5.1(h) presents representative imaging of a macroscopic region showing a dark contour indicative of liquid thickness that matches the SPP coupling condition at a given angle. By sweeping the incidence angle (while maintaining the same wavelength of the source), one can then obtain resonant curves which correspond to contour lines where the incident plane wave couples to SPP schematically shown in the deformed TLDF surface in Fig.5.1(c).

In practice, thin film's interface can be deformed by leveraging the fact that the liquid-gas surface is sensitive to external stimuli (see [OKM09] and references within). Specifically, in this work we take advantage of the optical absorption of the metal substrate which already supports SPP excitations in order to stimulate also the thermocapillary effect [Pea58], which have been extensively studied over the last decades [RAA$^+$03, CHT$^+$90, Sin17]. The thermocapillary effect is a special case of the Marangoni effect [Mar71]) [dGDQ13], and is manifested by thermocapillary flows and deformation of a TLDF due to spatial variations of the surface tension. The latter emerges due to nonuniform temperature distribution of the metal surface and subsequently also of the liquid-gas interface. In our work we apply heating beams of various intensities and spatial distributions and apply the k-space or real space imaging methods to construct a detailed local thickness measurement as well as topography maps with sub-nanometer sensitivity along the vertical direction.

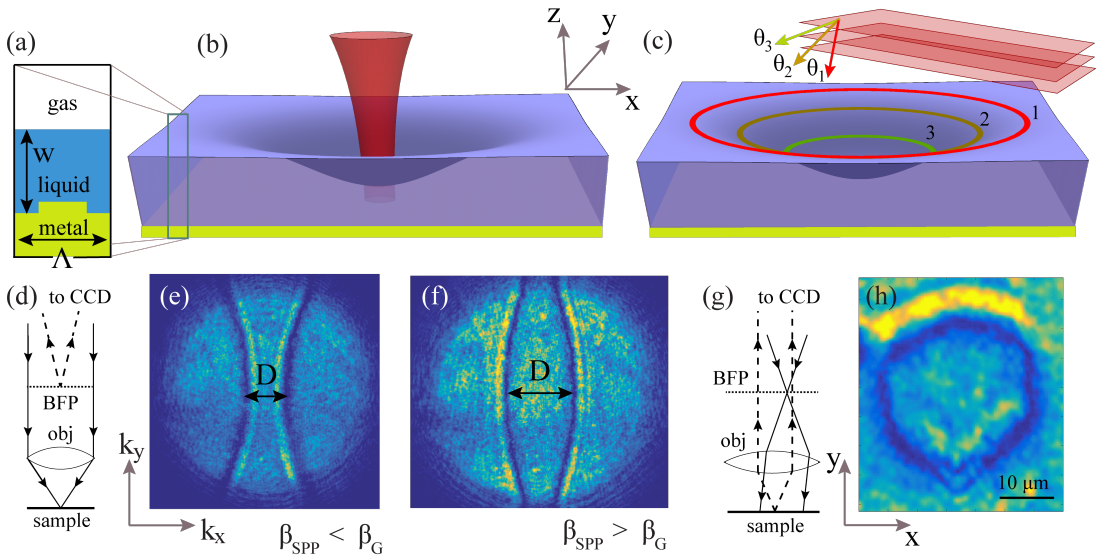

Figure 5.1: (a) The system under study; metal grating of period Λ covered with a bilayer of TLDF of local thickness w and gas. (b) The probing beam in the k-space method is a focused Gaussian beam which illuminates small (diffraction limited) spatial region; (c) the probing beam in real-space imaging method is a plane wave of fixed directionality which covers a macroscopic region. (d,g) The corresponding schemes highlighting the key differences between the profilometry methods. (e,f) Experimental representative images of the BFP with a dark arcs indicative of the resonant coupling angles to SPP for the regimes $\beta_{SPP} < \beta_G$ (e) and $\beta_{SPP} > \beta_G$ (f), respectively. (h) Experimental representative image of a resonant contour representative of a TLDF thickness which meets the coupling condition to an SPP at a given incident angle. By sweeping the angle of incidence ($\theta_{1,2,3}$ in (c)) of a given light source the coupling to SPP takes place at resonant contours ($1,2,3$ in (c)).

5.1.1 Coupling of SPP into grating covered with dielectric

Grating coupling is a common method to couple SPP to a metal surface (see [Hom06] and references within). Assuming a plane wave with a wave vector component parallel to the grating, $\vec{\beta}_I$, is made incident on a metal surface with a grating of period Λ, gives rise to a series of diffracted waves with wave vectors given by $\vec{\beta}_I + N\vec{\beta}_G$, where $\beta_G = (2\pi/\Lambda)\,\hat{k}_x$ is the grating vector which is perpendicular to the grating grooves (aligned along the y direction) and N is the diffraction order. The diffracted waves along the interface can couple to an SPP mode provided the following momentum balance equation holds [H.R13]

$$\beta_I + N\beta_G = \mathrm{Re}\,(\beta_{SPP})\,, \tag{5.1}$$

where $\beta_I = k_0 \sin(\theta)$, $\beta_{SPP} = k_0\sqrt{\varepsilon_m\varepsilon_d/(\varepsilon_m+\varepsilon_d)}$ is the SPP momentum [H.R13]. Here, θ is the resonance coupling angle of an incoming light, $k_0 = 2\pi/\lambda$ is the magnitude of a wave number vector in free space of wavelength λ, and $\varepsilon_{m,d}$ stand for the dielectric constants of metal and dielectric, respectively. Inserting the definitions of β_I, β_G and β_{SPP} into Eq.(5.1) yields the following expression for the resonant coupling angle, θ,

$$\sin(\theta) = \sqrt{\frac{\varepsilon_m}{\varepsilon_m + n_d^2}} - \frac{\lambda N}{\Lambda n_d}. \tag{5.2}$$

The latter implies that changes of the dielectric index, $n_d = \sqrt{\varepsilon_d}$, lead to changes of the resonant angle. In particular, in a case of a thin film that covers a metal grating, described in Fig.5.1(a), changes of the TLDF thickness lead to changes of the effective index of the dielectric. Qualitative description can be obtaing by treating the TLDF and air bilayer as a single media with a depth averaged index distribution obtained by integrating along the normal direction to the metal [GK07] allows in principle to determine the thickness based on the measured values of the resonant coupling angle. For quantitative description we turn to numerical simulation [Inc].

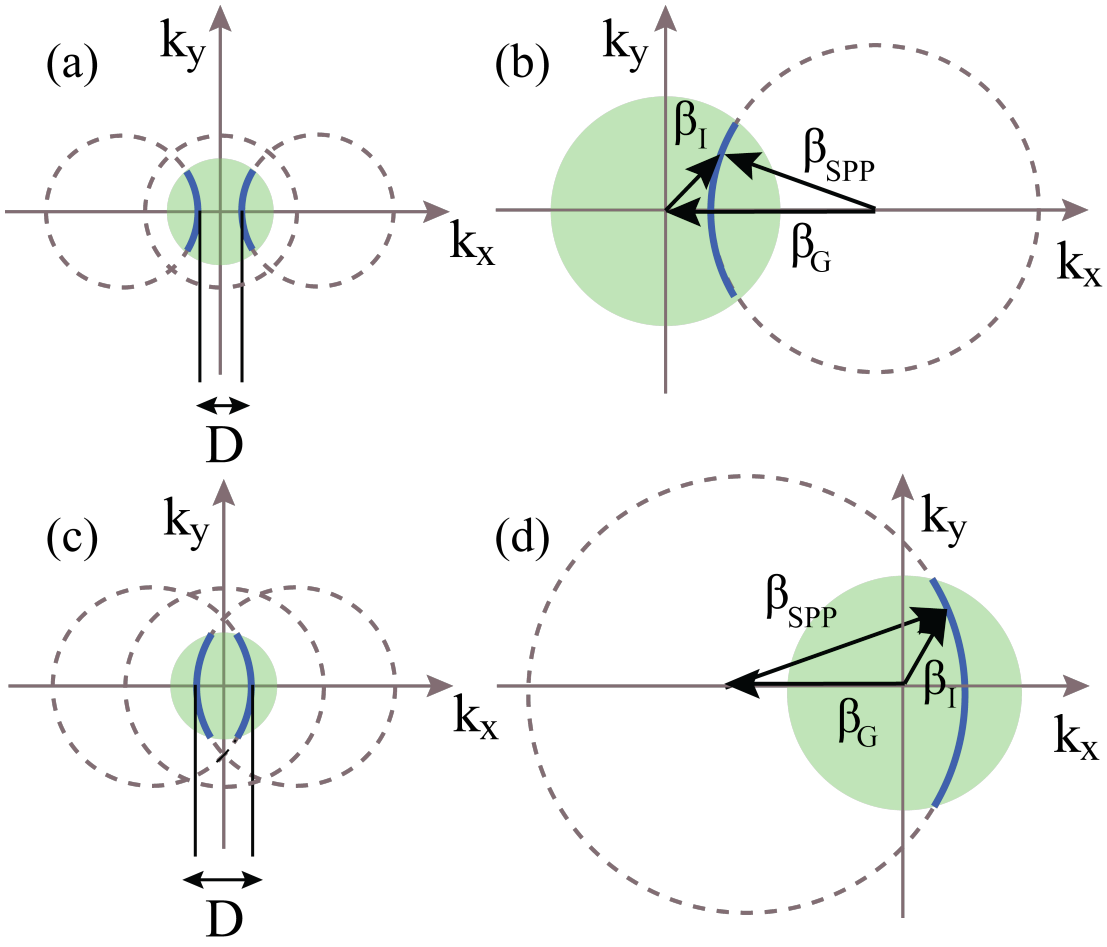

Figure 5.2: Schematic description of the momentum conservation relation that describes coupling of an incident light into SPP mode that propagates on a metal grating covered with TLDF. The momentum of the SPP mode, β_{SPP}, is equal to the radius of the dashed circles and is larger than the radius of the dashed disk, which describes the set of available momenta of an incident light β_I. (a,c) Present the allowed SPP states (dark arcs) formed by an intersection of the incident directions with the shifted SPP momenta for the two regimes $\beta_{SPP} < \beta_G$ and $\beta_{SPP} > \beta_G$. (b,d) Present the momentum balance for two regimes where the excited SPP mode carries in-plane momenta in the direction opposite (b) and parallel (d) to the in-plane momentum component of the incident light.

The distance between the dark arcs, D, described schematically in Fig.5.2 and also experimentally in Fig.5.1(e,f) is expressed via the resonant coupling angle via

$$\theta = \sin^{-1}(D/2k_0). \tag{5.3}$$

The corresponding thickness value of TLDF at the coupling region can then be inferred from the one to one relation between the dielectric thickness and the coupling angle, described in Fig.5.3.

It is instructive to mention that a small change of the thin film thickness induces much stronger effect on an SPP mode than on an FP (Fabry-Perot) mode, commonly used in white light microscopy. In particular, considering the maximal value of the ratio s, defined as $s \equiv \Delta R/\Delta w$ where Δw is the change of thickness whereas ΔR is the corresponding change of reflectivity, for FP and SPP resonances respectively, is given by $s^{FP}_{max} = \Delta R^{FP}_{max}/(\lambda/4n_l)$ and $s^{SPP}_{max} = \Delta R^{SPP}_{max}/\Delta w(\Delta\theta_{1/2})$. Here, $\lambda/4n_l$ is the change of the dielectric thickness that corresponds to a maximal shift of reflectivity given by $\Delta R^{FP}_{max} = 4r^2/(1+r)^2$ where $r = |(n_g - n_l)/(n_g + n_l)|$ is the Fresnel normal reflection coefficient [Zan13]; $\Delta w(\Delta\theta_{1/2})$ is the change of thickness which corresponds to twice the width of the angular half-width depth, $\Delta\theta_{1/2}$, of the corresponding angular-thickness curve. Assuming $\Delta R^{SPP}_{max} = 1$, and furthermore utilizing the values $n_g = 1$, $n_l = 1.39$, $\lambda = 785$ nm and $\Delta\theta_{1/2} = 4^o$ and the corresponding $\Delta d(\Delta\theta_{1/2}) = 15$ nm, yields $s^{SPP}_{max}/s^{FP}_{max} \simeq 15$.

5.1.2 Thin film equation for liquid deformation

The free surface of the thin film of a Newtonian fluid of viscosity μ and stress tensor τ_{ij} satisfies the following stress balance equation [EML87]

$$\tau_{ij} n_j = \sigma n_i \vec{\nabla} \cdot \hat{n} - \vec{\nabla}_{\parallel} \sigma; \quad i,j = x,y,z \tag{5.4}$$

where, σ is the surface tension, $\vec{\nabla}_{\parallel}$ stands for a gradient with respect to the in-plane coordinates (y,z) and $\vec{\nabla}\cdot\hat{n}$ is the divergence of the normal which is defined as the negative of the mean extrinsic curvature of the free interface. Assuming that the surface tension depends linearly on the temperature via [Lev62]

$$\sigma(T) = \sigma_0 - \sigma_T \Delta T; \quad \Delta T \equiv T - T_0, \tag{5.5}$$

where σ_T is the so-called Marangoni constant Applying low Reynolds number and thin film assumptions (i.e. lubrication approximation) [How05], for the Navier-Stokes equation [EML87], allows to drop the in-plane derivatives relative to the normal derivative and drop the inertial terms, and together with the thin film limit of the matching conditions, Eq.(5.4),[ODB97] and upon linearization [RYF18] yields the following equation for the thin film deformation η

$$\frac{\partial \eta}{\partial t} + D_\sigma \nabla_{\parallel}^4 \eta = \frac{\sigma_T h_0^2}{2\mu} \nabla_{\parallel}^2 T^m; \quad D_\sigma \equiv \sigma_0 h_0^3/(3\mu). \tag{5.6}$$

The latter includes the effects of surface tension and thermocapillarity, doesn't include effects of gravity which are negligible on a microscale and expected to emerge on a much larger scales comparable to the capillary length [dGDQ13], and doesn't include the effect of non-retarded van der Waals interaction can be neglected for films with thickness above 100 nm [Isr11]. Furthermore, we have assumed a thin film and small Biot number [RYF18] which implies that the temperature of the free surface is identical to the temperature field in the metal, T^m, which is governed by the following 2D equation

$$\frac{\partial T^m}{\partial t} - D_{th}^m \nabla_{\parallel}^2 T^m = \frac{\Delta T}{I_0 \tau_{th}} \chi I; \quad \chi \equiv \frac{\alpha_{th}^m d^2 I_0}{k_{th}^m \Delta T}. \tag{5.7}$$

Here, the superscript m stands for quantities in the metal, I is an optical intensity of typical strength I_0, $D_{th}^m = k_{th}^m/(\rho^m c_p^m)$ is the heat diffusion coefficient; ρ^m, c_p^m, k_{th}^m, α_{th}^m are the mass density, specific

heat, heat conductance, and optical absorption coefficient, respectively; $\tau_{th} = d^2/D_{th}^m$ is the typical time scale; d is the typical length scale along the in-plane direction; χ is the dimensionless intensity of the heat source. Assuming, quasistatic distribution of the temperature field, which expected to hold to a great degree of accuracy due to short heat diffusion time relative to the thin film deformation time, especially on metal surfaces allows to neglect the time derivative in Eq.(5.7) leading to [RYF18]

$$\frac{\partial \eta}{\partial t} + D_\sigma \nabla_\parallel^4 \eta = -\frac{\sigma_T h_0^2}{2\mu} \frac{\Delta T}{I_0 d^2} \chi I, \tag{5.8}$$

where the minus (positive) sign of the source term indicates decrease (increase) of local thickness for positive (negative) Marangoni constant. Scaling to dimensionless variables $t \to \tau_l t$ where $\tau_l = d^4/D_\sigma$, $\vec{r}_\parallel \to (\tau_{th} \cdot D_\sigma^{1/4})\vec{r}_\parallel$, $\eta \to h_0 \eta$ and $I \to I/I_0$ yields

$$\frac{\partial \eta}{\partial t} + \nabla_\parallel^4 \eta = -\mathrm{Ma} \cdot \chi \cdot \frac{\tau_l}{\tau_{th}} I/2. \tag{5.9}$$

where $\mathrm{Ma} \equiv \sigma_T \Delta T h_0/(\mu D_{th})$ is the dimensionless Marangoni number which represents the ratio between the surface tension stresses due to the thermocapillary effect, and dissipative forces due to fluid viscosity and thermal diffusivity.

5.2 Results

5.2.1 Numerical results of the resonant coupling angle as a function of liquid thickness

Fig.5.3 presents simulation results of an incident plane wave coupling into propagating SPP modes on a metal grating covered with a TLDF, by employing a commercial-grade simulator based on the finite-difference time-domain method [Inc]. The key parameters of the simulation domain, presented schematically in Fig.5.1(a), are: incoming plane wave of wavelength $\lambda = 785$

nm, grating periodicity $\Lambda = 600$ nm, gold dielectric function at corresponding wavelength $\varepsilon_m = -22.85 + 1.4245i$ [aC72], dielectric index $n_l = 1.39$ which corresponds to the refractive index of silicone oil [fis]. Fig.5.3(a) presents the resonant coupling angle θ, into a pure SPP mode and higher order guided mode, as a function of the dielectric thickness w. Both curves are strictly decreasing functions and therefore can be used to construct an inverse function where w serves as an argument, which is of importance for the interpretation of the experimental results below. Importantly, the SPP curve presented in Fig.5.3(a) admits both positive and negative angles which correspond, respectively, to counter- and co-propagating SPP modes; i.e. for sufficiently thin (thick) films the SPP mode propagates in a direction opposite (parallel) to the in-plane component of the incident light. These two regions are separated by an angular band-gap centered at the normal incidence angle $\theta = 0$, presented in Fig.5.3(b), which is reminiscent of the band gap observed near normal incidence conditions on a metal gratings without a dielectric layer [PHSF07] due to destructive interference of the left and right propagating SPP modes. The filled curves in Fig.5.3(a) present the corresponding sensitivity, defined as $dw/d\theta$, for the SPP and the higher order guided mode. While the SPP curve admits highest sensitivity around thickness 100 nm and practically vanishes for thickness above 600 nm, the guided mode which doesn't couple at low thicknesses and admits highest optical intensity closer to the dielectric top surface, acquires highest sensitivity at around 400 nm and vanishes for dielectric thickness around $1\mu m$. The latter reflects the fact that for low thickness values the incoming plane wave couples to a pure SPP mode with highest optical intensity on the metal surface (presented in Fig.5.3(c)), whereas for a large enough thickness the incident light couples also into higher order guided mode with highest optical intensity at some finite distance from the metal surface, presented in Fig.5.3(d), which makes it more sensitive to thickness changes of thicker films (see also [HB07] for optical intensity distribution along the vertical direction in dielectric-loaded surface plasmon-polariton waveguides). Since SPP and guided modes propagating in a dielectric multilayer near a metal can be regarded as a particular waveguide mode [HJL$^+$17] with dispersion relation set by the

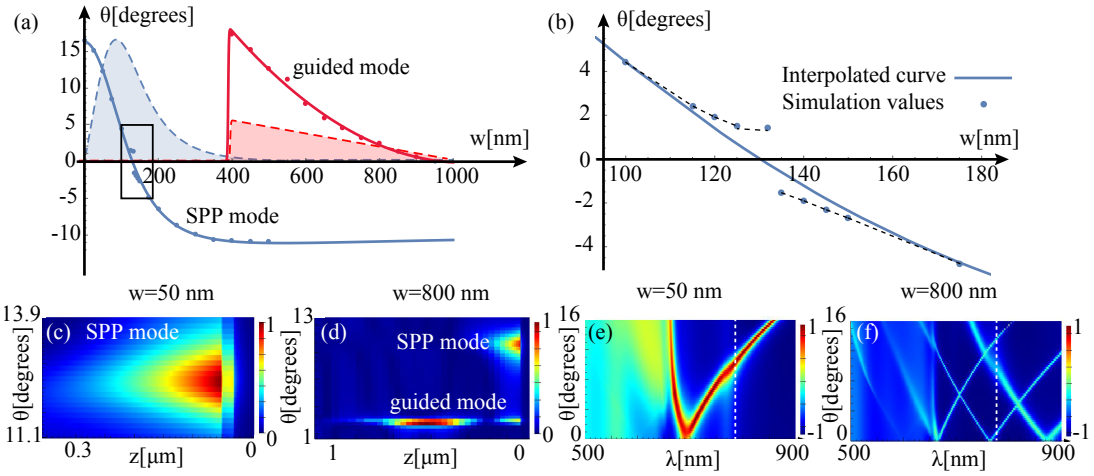

Figure 5.3: (a) Discrete values and smooth interpolating curves that describe the resonant coupling angle as a function of TLDF thickness for pure SPP and higher order guided mode, accompanied by the corresponding normalized sensitivity curves (filled). (b) Presents the angular band-gap formed around the normal incidence point within the black rectangular in (a). (c,d) Present the electrical field intensity along the vertical direction against the incidence angle colormap whereas (e,f) present the dispersion relation, both for thin (50 nm) and thick (800 nm) films.

constructive interference condition [KR74], it follows that additional higher order guided modes must emerge at even higher thickness values of TLDF.

Fig.5.3(e) presents the dispersion relation of the basic SPP mode showing a single curve where the right and left branches correspond, respectively, to counter- and co-propagating modes relative to the in-plane component of the incident plane wave. The dashed vertical line at 785 nm intersects with the right branch indicating that given conditions facilitate coupling only to basic counter propagating SPP mode at resonant coupling angle 12.28 degrees. Fig.5.3(f) presents additional higher modes that emerge at thicker film of thickness 800 nm and a dashed vertical line which intersects with a left (co-propagating) branch of the basic SPP curve at 11.12 degrees and with the right branch of the higher order guided mode at 2.51 degrees.

5.3 Experimental setup

Sample preparation

To provide a SPP transducer for coupling sensing SPPs, a square grating with 600 nm period and 30 nm depth were made depositing 200 nm gold onto a nanoimprinted grating template with a chemical vapor deposited silicon dioxide layer of 2 micrometers on a silicon substrate.

To implement the working thin fluid layer, silicone oil (Fisher) was spun onto the grating by repeated intervals of spin coating at 10,000 rpm. Baseline thickness of the prepared fluid layer was measured by spectral reflectance to be on average 176 nm by a separate optical profilometer (Filmetrics F20). A complete spin curve for 3-12 spins was obtained to prepare baseline average fluid thickness from 175 to 700 nm.

Optical setup

An epi collection microscope was used to both drive thermocapillary flows and image the fluid response (Olympus). A 488 nm argon ion laser was collimated and passed through a 50x microscope objective (Mitutoyo), and focused to a point with 1.5 micron width (FWHM). Direct absorption by the gold was used to generate a temperature gradient and support the thermocapillary flows in the fluid around the absorption point.

An imaging 785 nm laser diode beam was used to excite SPPs along the grating, and was placed onto the argon beam path using a dichroic mirror. The light was delivered to the microscope objective in two configurations: (1) colinear with the pump beam as a plane wave and (2) focused to the objective back focal plane (BFP) and delivered to the sample as a plane wave. In the first configuration, the imaging laser was then epi collected and the BFP is imaged to measure the angular spectrum up to the objective numerical aperture; the input angles satisfying the SPP momentum conditions appear as absorption lines in the angular spectrum. Changes in the momentum condition owing to the thickness change at the point of heating

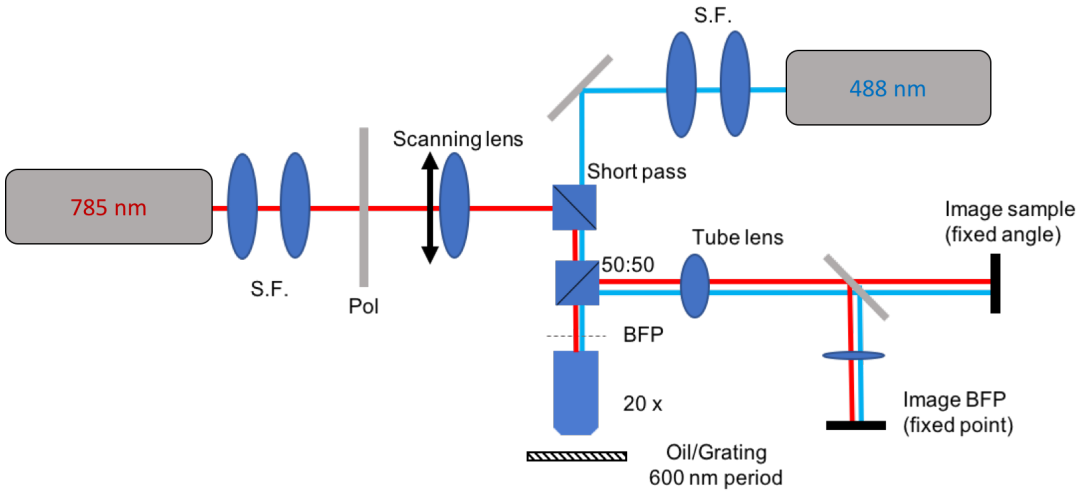

Figure 5.4: Schematic description of an experimental system we used for both direct and *k*-space measurement. The low power 785 nm probing beam and the higher power 488 nm heating beam were brought to the same optical path. Upon reflection from the sample the light was collected by the CCD. BFP - back focal plane, P - Polarizer, BS - 50:50 beam splitter.

were visualized as shifts in the resonance angle, and relaxation dynamics of the thermocapillary induced deformations could be visualized. In the second configuration, the collimated imaging laser was passed through a lens (f = 40 cm) on a lateral translation stage and focused onto the BFP for Kohler illumination. Lateral displacements of the lens shifted the focus across the BFP, thus shifting the plane wave angle of incidence at the grating. The collected light was imaged by the microscope tube lens for direct observation of the grating surface and regions with fluid thickness matching the SPP condition at a given angle of incidence could be observed to darken according to resonant absorption. Because the large thickness range in the fluid layer after thermocapillary flow, sweeping of the illumination angles allowed visualization of resonant contours of the corresponding to level regions with thickness supporting SPR resonance at the given angle.

5.4 Experimental results

In our experiments we apply two different laser sources in order to heat the sample and probe the deformation of the free interface; an Argon laser (488 nm) which heats the metal and invokes the thermocapillary effect accompanied by the deformation of the TLDF, and a Helium-Neon laser (785 nm) which provides angular and spatial information upon reflection from the sample. Our optical setup aimed to bring the two light sources on the same optical path and collect the reflection of the probing beam into the CCD. See supplemental information for more details.

5.4.1 K-space imaging

Fig.5.5(a) presents experimental results of TLDF thickness as a function of time at the illumination spot due to three different optical heating powers. Before the heating beam is applied ($t < 0$), all three experiments show near a constant thickness values whereas at later times during a time period of 20 seconds the fluid thickness is reduced due to the thermocapillary effect. After the beam is switched off all curves show an increase of film thickness and relaxation towards the initial state. As expected higher optical powers imply lower thickness values, however TLDF thicknesses due to highest intensity beams A, B show a very small difference relative to the distance from curve C. The latter is indicative of a rupture process in the TLDF which exposes disk-shaped regions of the substrate shown in white-light microscopy images in Fig.5.5(b-d) for a similar optical power and thicker 0.5 μm silicone oil film. Indeed, since the growing rate of the rupture is expected to decrease over time, similar to the minimal TLDF thickness as a function of the optical power in thicker films [Wed14]), we expect similar TLDF configurations in experiments A, B after the beam is switched off and consequently similar relaxation dynamics. Fig.5.5(e) presents thickness measurement of TLDF at much lower optical power 6 μW which allowed to capture the dynamics of TLDF during the operation of the heating beam. During

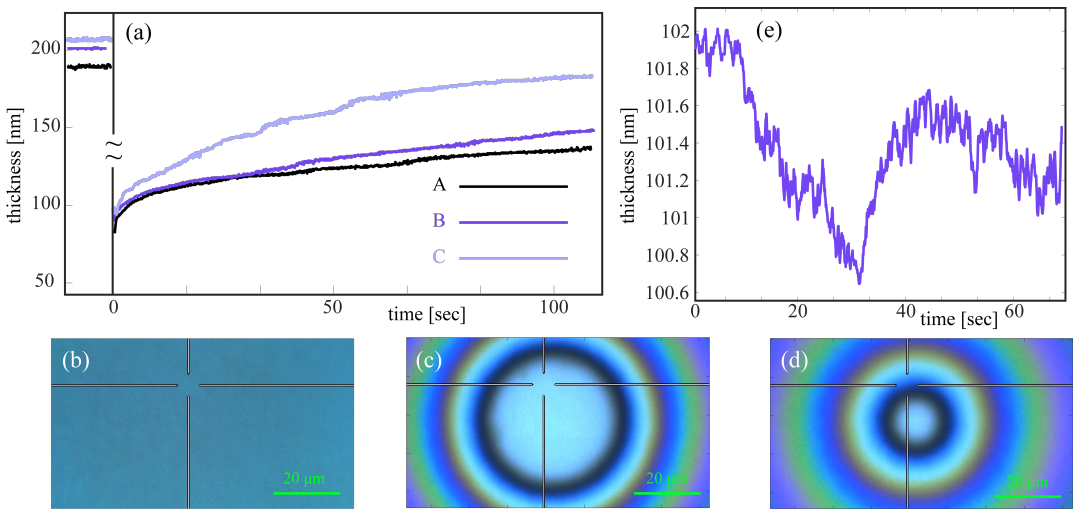

Figure 5.5: (a) thickness at central point of a heating beam as a function of time for three different optical powers of the Argon beam (A) 34.57 mW, (B) 17.96 mW and (C) 1.79 mW. (b,c,d) Present two-dimensional white light microscopy images of the rupture process of the TLDF at three moments of time: (b) before optical heating, (c) 10 sec after the heating is switched off and (d) 30 sec after the heating is switched off. (e) Presents thickness as function of time due to 20 sec illumination of a 6 μW low power heating beam at times $10-30$ sec, and thin film healing after the beam is switched off at $t = 30$ sec.

the operation of the heating beam at times $10-30$ sec, TLDF shows a decrease in its thickness, whereas at later times ($t > 30$ s) it shows a healing process characterized by an increase of its thickness, qualitatively similar to the healing process occurring at higher powers as described in Fig.5.5(a). Notably, the thickness change of TLDF occurs at a sub-nanometer scale and over a long period of time - of the order of seconds.

Such a large time scale allows to rule out other thermally driven effects such as the thermo-optical effect which is governed by heat diffusion processes and operates on a much shorter time scales of order of magnitude of micro-seconds (see methods section for an estimate).

5.4.2 Real-space imaging

Fig.5.6 presents experimental results of TLDF equal-height contours, the corresponding interpolated free surfaces and numerical simulation results due to two types of heating illumination and temperature distribution on the metal surface. In particular Fig.5.6(a,c,e) and Fig.5.6(b,d,f)

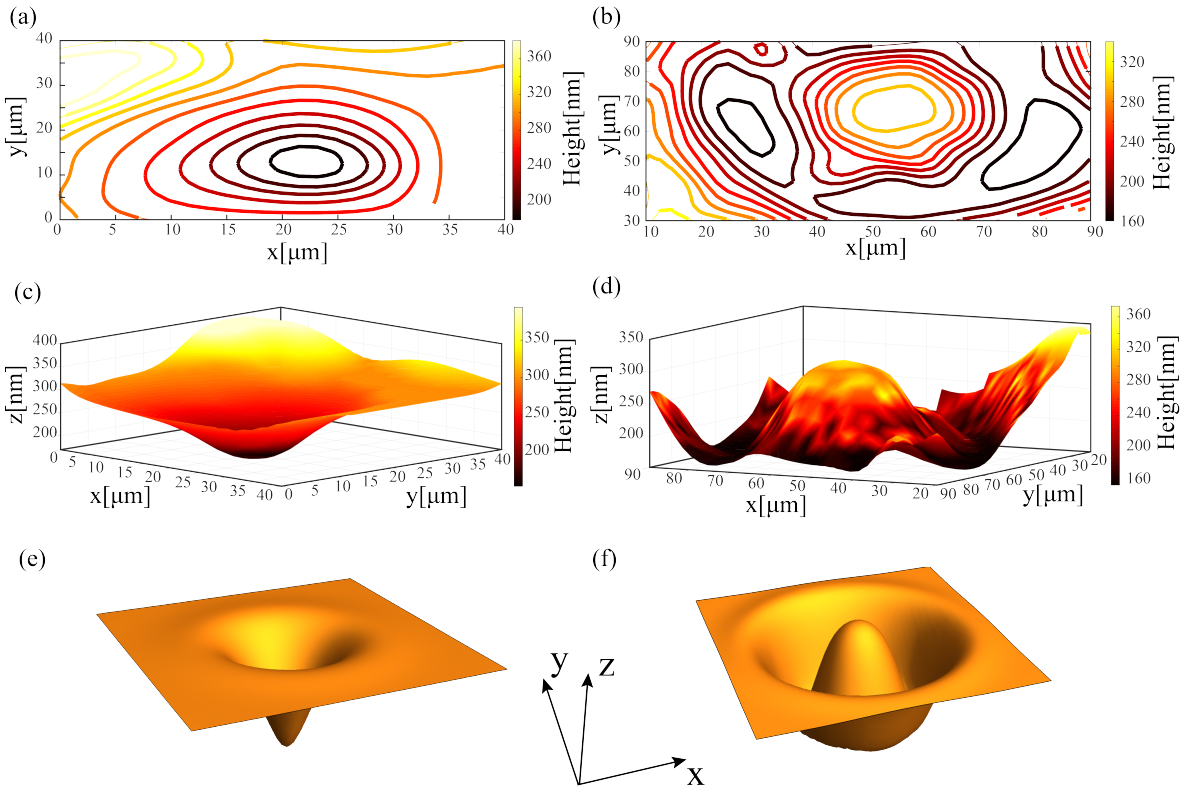

Figure 5.6: (a,c) and (b,d) present contour maps and interpolated 3D topography maps due to focused and donut-shaped illumination pattern. (e,f) Numerical results presenting thin film deformation solution of non-dimensional Eq.(5.9) for an intensity of the type $I(r) = e^{-(r-r_0)^2}$; (e) $r_0 = 0$ Gaussian source centered at the origin which gives rise to a centered dimple, (f) $r_0 = 5$ Gaussian source with maximal intensity on a circle of radius r_0 resulting in a drop-like structure. The size of the domain along the in-plane $y-z$ directions is 20×20 and the maximal value of the deformation is 0.06.

correspond, respectively, to the cases where the temperature sources are concentrated in a small region of diameter around 0.65 μm and a donut-shaped region of inner diameter around 40 μm. Fig.5.6(a,b) present experimental images of a series of dark resonant contours, which correspond to different equal-height contours of the TLDF free surface, obtained by sweeping the corresponding incident angles and capturing the reflected light from the sample. Together with Fig.5.6(c,d) which present the corresponding interpolated 3D topography map, both show lower film thickness at regions of highest optical intensity. The step in the illumination angle sweep is 0.77 degrees per step, and then for each value of resonant angle we used the theoretical curve to determine the thickness of the oil TLDF. We applied Gaussian smoothing filter of 1.5 pixels (8.6 μm) to all images to remove the noisy features in the contours. The compact point-like heating spot source introduces a maximal temperature field at the center of the illumination spot and triggers thermocapillary flows that drive the fluid towards regions with a lower temperature and a higher surface tension, which results in an indentation of a fluid profile at the center. By applying a donut-shaped illumination, thermocapillary flows similarly drive the fluid from a donut-shaped region towards the center, which in contrast to the localized heating source results in a bulge at the central region. It is instructive to mention that the slope of the TLDF in our experiments was sufficiently low and therefore the corresponding effects of free interface curvature on the coupling angle is small. Indeed, as seen from Fig.5.6(c) the mean slope is around $\Delta z/\Delta x = 100nm/20\mu m = 5 \cdot 10^{-3}$, which is smaller than the critical value $8 \cdot 10^{-2}$ predicted by the analysis from Fig.5.6.

5.5 Conclusion

In this work we presented two novel profilometry methods to measure thickness of TLDF and applied them to determine thin film dynamics driven out of equilibrium by an optically induced thermocapillary effect. The imaging methods presented in our work are complementary

in a sense that while k-space imaging provides thickness values as a function of time at a small region, real-space imaging provides a resonant contour indicative of a specific height over a large area of few hundreds of microns. Both methods admit immediate generalizations and can be utilized to obtain more complete probing by introducing higher speed sweeping mechanisms (e.g. translation stages); the k-space imaging can be extended to provide thickness information along spatial segments that can cover 2D regions, whereas direct-imaging can in principle capture faster process. Our methods open a door for future studies where thickness changes of TLDF monitored on a nanometer or a sub-nanometer scale would be indicative of various physical processes such as instabilities due to electrohydrodynamical [Her99, STARU01] and electrostatic [Mor03] effects, dispersion forces [Rei92], chemical changes such as light-driven photoisomerization from trans- to cis-isomer states [RBN95], and heat-transfer during evaporation from non-uniform films [LWP94]. In addition, the methods are applicable to study phase transitions in thin polymer films [WZW95] and light-induced reversible thickness [YTG$^+$06] without the need to employ, respectively, x-ray reflectivity and neutron reflectometry methods. Importantly, our methods aren't compromised if an additional thin layer of material is added on top of the metal grating to achieve desired surface properties, which in principle allows to study basic problems such as wetting and spreading of thin films on different substrates. By applying our imaging method we demonstrated that light induced thermocapillary effect can be utilized to create dynamical structures such as droplets which may be useful for future applications in nanoscopy [LKK09, Wan11, Kri13] and various bio-applications such as cells communication.

This chapter is taken from material submitted for review and publication, authored by Rubin, Shimon; Hong, Brandon; and Fainman, Yeshaiahu. The dissertation author was primary co-author of this manuscript with Shimon Rubin, and Yeshaiahu Fainman was the principal investigator.

Bibliography

[aC72] Johnson and Christy. 1972.

[AG13] A. Arbabi and L.L. Goddard. Measurements of the refractive indices and thermo-optic coefficients of si3n4 and sio x using microring resonances. opt. lett, 2013.

[aIW03] E.Katz and I. Willner. *biomolecular interactions at conductive and semiconductive surfaces by impedance spectroscopy: routes to impedimetric immunosensors, DNA-sensors, and,*. Electroanalysis, 2003.

[aJH08] J.Dostálek and J. Homola. Surface plasmon resonance sensor based on an array of diffraction gratings for highly parallelized observation of biomolecular interactions,. *Sens. Actuators B Chem*, 129:303–310, 2008.

[AMR11] J.L. Arlett, E.B. Myers, , and M. L. Roukes. Comparative advantages of mechanical biosensors,. *Nat. Nanotechnol*, 6:203–215, 2011.

[AMS+11] D. Andre, M. Meiler, K. Steiner, C. Wimmer, T. Soczka-Guth, , and D. U. Sauer. Characterization of high-power lithium-ion batteries by electrochemical impedance spectroscopy. i. experimental investigation,. *J. Power Sources*, 196:5334–5341, 2011.

[aNP07] J.S.Daniels and N. Pourmand. Label-free impedance biosensors: Opportunities and challenges.,. *Electroanalysis*, 19:1239–1257, 2007.

[AOA+16] I. August, Y. Oiknine, M. AbuLeil, I. Abdulhalim, and A. Stern. Miniature compressive ultra-spectral imaging system utilizing a single liquid crystal phase retarder. *Sci. Rep*, 6:23524, 2016.

[BA02] C.A. Balaras and A.A. Argiriou. Infrared thermography for building diagnostics. *Energy Build*, 34(2):171–183, 2002.

[Bak14] M.J. Baker. Using fourier transform ir spectroscopy to analyze biological materials. *Nat. Protoc*, 9:1771–1791, 2014.

[Bar85] T. Barnes. Photodiode array fourier transform spectrometer with improved dynamic range. *Appl. Opt*, 24:3702–3706, 1985.

[Bar05] G. Bartal. Physical review letters, 2005.

[BB15] J. Bao and M.G. Bawendi. A colloidal quantum dot spectrometer. *Nature*, 523:67, 2015.

[BLB+13] T. Bryan, X. Luo, P.R. Bueno, , and J. J. Davis. An optimised electrochemical biosensor for the label-free detection of c-reactive protein in blood.,. *Biosens. Bioelectron*, 39:94–8, 2013.

[Bon09] Daniel Bonn. Wetting and spreading. *Reviews of modern physics*, 81(2):739, 2009.

[Bre12] P. Breuil. Multisensors: Measurements and behavior models,. *Chem. Sens. Biosens*, 211(233), 2012.

[CCW+07] H.P. Chiang, C.-W. Chen, J.J. Wu, H.L. Li, T.Y. Lin, E.J. Sánchez, and P.T. Leung. Effects of temperature on the surface plasmon resonance at a metal–semiconductor in-terface. thin solid films, 2007.

[CHT+90] A.M. Cazabat, F. Heslot, S.M. Troian, , and P. Carles. Fingering instability of thinspreading films driven by temperature gradients. *Nature*, 346(6287), 1990.

[Coa07] E.Le Coarer. Wavelength-scale stationary-wave integrated fourier-transform spectrometry. *Nat. Photonics*, 1:473–478, 2007.

[dGDQ13] P.-G. de Gennes, , and F.Brochard-Wyart D. Quere. *Capillarity and Wetting Phenomena: Drops, Bubbles, Pearls, Waves*. Springer Science and Business Media, 2013.

[EML87] L.D.Landau E. M. Lifshitz. In *Fluid Mechanics, Course 6 of Theoretical Physics*, volume 6. 1987.

[EPL+13] A.T. Exner, I. Pavlichenko, B.V. Lotsch, G. Scarpa, and P. Lugli. Low-cost thermo-optic imaging sensors: A detection principle based on tunable one-dimensional photonic crystals. *ACS Appl. Mater. Interfaces*, 5(5):1575–1582, 2013.

[Fan14] S. Fang. An integrated system for regional environmental monitoring and management based on internet of things. *IEEE Trans. Ind. Inform*, 10:1596–1605, 2014.

[FB12] J.R. Ferraro and L.J. Basile. *Fourier transform infrared spectra: applications to chemical systems*. Academic press, 2012.

[fis]

[FKP+95] G. Flatgen, K. Krischer, B. Pettinger, K. Doblhofer, H. Junkes, , and G. Ertl. *Science*, 269:668, 1995.

[FSPF16] L.M. Freeman, A. Smolyaninov, L. Pang, and Y. Fainman. Simulated raman correlation spectroscopy for quantifying nucleic acid-silver composites. *Sci. Rep*, 6, 2016.

[FST08] K.J. Foley, X. Shan, , and N. J. Tao. Surface impedance imaging technique.,. *Anal. Chem*, 80:5146–51, 2008.

[GH07] P.R. Griffiths and J.A.De Haseth. *Fourier transform infrared spectrometry*, volume 171. John Wiley and Sons, 2007.

[GK07] C.T.Campbell G. Kim. Spr microscopy and its applications to high-throughput analyses of biomolecular binding events and their kinetics. *Biomaterials*, 28(15):2380–2392, 2007.

[Gro01] James B. Grotberg. Respiratory fluid mechanics and transport processes. In *Annual review of biomedical engineering*, volume 3, page 421–457. 2001.

[HB07] Tobias Holmgaard, , and Sergey I. Bozhevolnyi. Theoretical analysis of dielectric-loadedsurface plasmon-polariton waveguides. *Physical Review B*, 75(24):245405, 2007.

[Her99] S. Herminghaus. Dynamical instability of thin liquid films between conducting media. *Physical review letters*, 83(12):2359, 1999.

[HF06] B. Henderson and G. F. *Imbusch, Optical spectroscopy of inorganic solids*, volume 44. University Press, Oxford, 2006.

[HJL$^+$17] W. Han, L. Jiang, X. Li, Q. Wang, S. Wang, J.and Lu Hu, and Y. Controllable plasmonic nanostructures induced by dual-wavelength femtosecond laser irradiation. *Scientific reports*, 7(1):17333, 2017.

[HML17] E. Huang, Q. Ma, and Z. Liu. Etalon array reconstructive spectrometry. *Sci. Rep*, 7, 2017.

[Hol00] G.C. Holst. Common sense approach to thermal imaging; spie optical engineering press, 2000.

[Hom03] J. Homola. Present and future of surface plasmon resonance biosensors.,. *Anal. Bioanal. Chem*, 377:528–39, 2003.

[Hom06] J. Homola, editor. *Surface Plasmon Resonance Based Sensors*. Springer, 2006.

[How05] S. Howison. *Practical Applied Mathematics: Modeling, Analysis, Approximation*, 38(18), 2005.

[HPM$^+$08] G.M. Hwang, L. Pang, E.H. Mullen, , and Y. Fainman. Plasmonic sensing of biological analytes through nanoholes,. *IEEE Sens. J*, 8:2074–2079, 2008.

[H.R13] H.Raether. *Plasmons on Smooth and Rough Surfaces and on Gratings*. Springer-Verlag Berlin, 2013.

[HSD10] E. Hwang, I.I. Smolyaninov, , and C. C. Davis. Surface plasmon polariton enhanced fluorescence from quantum dots on nanostructured metal surfaces.,. *Nano Lett*, 10:813–20, 2010.

[HSP+15] B. Hong, A. Sun, L. Pang, A.G. Venkatesh, D. Hall, and Y. Fainman. Integration of faradaic electrochemical impedance spectroscopy into a scalable surface plasmon biosensor for in tandem detection. *Opt. Express*, 23(23):30237–30249, 2015.

[HWKS89] W. Hickel, , and D.Kamp W. Knoll. Surface. Plasmon microscopy. *Nature*, 339:186, 1989.

[HYG99] J. Homola, S.S. Yee, and G. Gauglitz. Surface plasmon resonance sensors. *Review. Sens. Actuators, B*, 54(1):3–15, 1999.

[IKH16] I. Ishimaru, N. Kawashima, and S. Hosono. Built-in hyperspectral camera for smartphone in visible, near infrared and middle infrared lights region (first report): trial products of beans-size fourier-spectroscopic line-imager and feasibility experimental results of middle infrared spectroscopic imaging. *SPIE Commer. Sci. Sens. Imaging Int. Soc. Opt. Photonics*, page 985504–985504, 2016.

[Inc] Lumerical Inc.

[Isr11] J.N. Israelachvili. *Intermolecular and Surface Forces*. Academic Press, Burlington, 2011.

[JBR+09] C.D.W. Jones, C.A. Bolle, R. Ryf, M.E. Simon, F. Pardo, V.A. Aksyuk, W.C. Lai, J.E. Bower, J.F. Miner, F.P. Klemens, and R.A.M.E.M.S. Cirelli. Thermal imager with optical readout, 2009.

[JH14] P.Kvasnicka J. Homola. Convenient method of micrometer-scale excitation of propagating surface plasmons by a focused laser beam. *Plasmonics*, 9(4):737–739, 2014.

[KLa35] W. Kossel, V. Loeck, , and H. Voges and, 1935.

[KPRA14] P.M. Kosaka, V. Pini, J.J. Ruz, and R. A. Detection of cancer biomarkers in serum using a hybrid mechanical and optoplasmonic nanosensor.,. *Nat. Nanotechnol*, 9:1047–53, 2014.

[KR74] H. Kogelnik, , and V. Ramaswamy. Scaling rules for thin-film optical waveguides. *Applied Optics*, 13(8):1857–1862, 1974.

[Kri13] Leonid A. Krivitsky. Locomotion of microspheres for super-resolution imaging. *Scientific reports*, 3:3501, 2013.

[Kru01] P.W. Kruse. Uncooled thermal imaging: Arrays, systems, and applications; spie press, 2001.

[LCG+06] U. Levy, K. Campbell, A. Groisman, S. Mookherjea, , and Y. Fainman. On-chip microfluidic tuning of an optical microring resonator,. *Appl. Phys. Lett*, 88:111107, 2006.

[Lev62] V.G. Levich. *Physicochemical Hydrodynamics*. Prentice hall, 1962.

[LGH+14] L. Liu, J. Guo, Y. He, P. Zhang, Y. Zhang, , and J. Guo. Study on the despeckle methods in angular surface plasmon resonance imaging sensors,. *Plasmonics*, 10:729–737, 2014.

[LKK09] C.-S. Lee, S.K. Kim, , and M. Kim. Ion-sensitive field-effect transistor for biological sensing.,. *Sensors*, 9:7111–31, 2009.

[Lof91] S. Lofas. Bioanalysis with surface plasmon resonance. *Sensors and Actuators B. 16 Chemical*, 5(1-4):79–84, 1991.

[LWP94] An-Hong Liu, Peter C. Wayner, , and Joel L. Plawsky. Image scanning ellipsometry for measuring nonuniform film thickness profiles. *Applied optics*, 33(7):1223–1229, 1994.

[LWW+12] J. Lu, W. Wang, S. Wang, X. Shan, J. Li, , and N. Tao. Plasmonic-based electrochemical impedance spectroscopy: application to molecular binding.,. *Anal. Chem*, 84:327–33, 2012.

[Mai07] S.A. Maier. Plasmonics: Fundamentals and applications. *Springer Science and Business Media*, 2007.

[Mar71] C.G.M. Marangoni. *Ann. Phys. Chem*, 219:337, 1871.

[MLL14] C. García-Ruiz M. López-López. Infrared and raman spectroscopy techniques applied to identification of explosives. *TrAC Trends Anal. Chem*, 54:36–44, 2014.

[Mor03] Mihai D. Morariu. Hierarchical structure formation and pattern replication inducedby an electric field. *Nature materials*, 2(1):48, 2003.

[MR08] Z. Movasaghi and S. Rehman. Fourier transform infrared (ftir) spectroscopy of biological tissues. *Appl. Spectrosc. Rev*, 43:134–179, 2008.

[MRR07] Z. Movasaghi, S. Rehman, and I.U. Rehman. Raman spectroscopy of biological tissues. *Appl. Spectrosc. Rev*, 42:493–541, 2007.

[NSB+10] M.P. Nezhad, A. Simic, O. Bondarenko, B. Slutsky, A. Mizrahi, L. Feng, V. Lomakin, and Y. Fainman. Room-temperature subwavelength metallo-dielectric lasers. *Nat. Photonics*, 4(6):395–399, 2010.

[NSC12] T.T. Nguyen, K.L. Sly, , and J. C. Conboy. Comparison of the energetics of avidin, streptavidin, neutravidin, and anti-biotin antibody binding to biotinylated lipid bilayer examined by second-harmonic generation.,. *Anal. Chem*, 84:201–8, 2012.

[ODB97] Alexander Oron, Stephen H. Davis, , and S. George Bankoff. Long-scale evolution of thin liquid films. *Reviews of modern physics*, 69(3):931, 1997.

[OKM09] R.V.Craster O. K. Matar. Dynamics and stability of thin liquid films. *Reviews of modern physics*, 81(3):1131, 2009.

[OOW+13] R. Ohno, H. Ohnuki, H. Wang, T. Yokoyama, H. Endo, D. Tsuya, , and M. Izumi. Electrochemical impedance spectroscopy biosensor with interdigitated electrode for detection of human immunoglobulin a.,. *Biosens. Bioelectron*, 40:422–6, 2013.

[Ost06] D. Ostrower. Optical thermal imaging–replacing microbolometer technology and achieving universal deployment. iii-vs, 2006.

[pBH13] T. Špringer, M. Bocková, , and J. Homola. Label-free biosensing in complex media: a referencing approach.,. *Anal. Chem*, 85:5637–40, 2013.

[PDG+14] C. Polonschii, S. David, S. Gáspár, M. Gheorghiu, M. Rosu-Hamzescu, , and E. Gheorghiu. Complementarity of eis and spr to reveal specific and nonspecific binding when interrogating a model bioaffinity sensor; perspective offered by plasmonic based eis.,. *Anal. Chem*, 86:8553–62, 2014.

[Pea58] J.R.A. Pearson, 1958.

[PHSF07] L. Pang, G.M. Hwang, B. Slutsky, and Y. Fainman. Spectral sensitivity of two-dimensional nanohole array surface plasmon polariton resonance sensor. *Appl. Phys. Lett*, 91(12):123112, 2007.

[Pin55] D. Pines. *Solid State Phys*, 1:367, 1955.

[PNF03] L. Pang, W. Nakagawa, and Y. Fainman. Fabrication of optical structures using su-8 photoresist and chemically assisted ion beam etching. *Opt. Eng*, 42(10):2912–2917, 2003.

[PPF05] D. Panasenko, S. Putilin, and Y. Fainman. Tunable spectral interferometry for broadband phase detection by use of a pair of optical parametric amplifiers. *JOSA B*, 22:922–929, 2005.

[PUS+12] A.D. Pris, Y. Utturkar, C. Surman, W.G. Morris, A. Vert, S. Zalyubovskiy, T. Deng, H.T. Ghiradella, and R.A. Potyrailo. Towards high-speed imaging of infrared photons with bio-inspired nanoarchitectures. *Nat. Photonics*, 6(3):195–200, 2012.

[QHL+16] Z. Qian, Y. Hui, F. Liu, S. Kang, S. Kar, and M. Rinaldi. Graphene–aluminum nitride nems resonant infrared de-tector. *Microsyst. Nanoeng*, page 2, 2016.

[QWC10] H. Qi, C. Wang, , and N. Cheng. Label-free electrochemical impedance spectroscopy biosensor for the determination of human immunoglobulin g,. *Microchim. Acta*, 170:33–38, 2010.

[RA12] E.F.J. Ring and K. Ammer. Infrared thermal imaging in. *Medicine. Physiol. Meas*, 33(3):33, 2012.

[RAA+03] G. Reiter, Sharma A, Casoli A, David MO, Khanna R, and Auroy P. Thin film instability inducedby long-range forces. langmuir, 1999-03.

[RAC+68] R. Ritchie, E. Arakawa, J. Cowan, , and R. Hamm. "surface-plasmon resonance effect in grating diffraction," phys. *Rev. Lett*, 21:1530–1533, 1968.

[Rae98] H. Raether. Surface plasmons on rough and smooth surfaces and on gratings,, 1998.

[RASC14] B. Redding, M. Alam, M. Seifert, and H. Cao. High-resolution and broadband all-fiber spectrometers. *Optica*, 1:175–180, 2014.

[RBN95] P. Rochon, E. Batalla, , and A. Natansohn. Optically induced surface gratings on azoaromaticpolymer films. *Applied Physics Letters*, 66(2):136–138, 1995.

[RDC17] G. Rateni, P. Dario, and F. Cavallo. Smartphone-based food diagnostic technologies. *A Review. Sensors*, 17:1453, 2017.

[Rei92] G. Reiter. *Phys. Rev. Lett*, 68:75, 1992.

[Rit57] R.H. Ritchie. *Phys. Rev*, 106:874, 1957.

[RLSC13] B. Redding, S.F. Liew, R. Sarma, and H. Cao. Compact spectrometer based on a disordered photonic chip. *Nat. Photonics*, 7:746–751, 2013.

[Rob91] J.M. Robinson. Fire from space: Global fire evaluation using infrared remote sensing. *Int. J. Remote Sens*, 12(1):3–24, 1991.

[Rog03] A. Rogalski. Infrared detectors: Status and trends. prog. quantum electron, 2003.

[Rog11] A. Rogalski. Recent progress in infrared detector technologies. infrared phys. *Technol*, 54(3):136–154, 2011.

[RSA11] L. Rodriguez-Saona and M. Allendorf. Use of ftir for rapid authentication and detection of adulteration of food. *Annu. Rev. Food Sci. Technol*, 2:467–483, 2011.

[RYF18] S. Rubin and Phys. Rev Y. Fainman. In *Lett.120*, page 243904. 2018.

[SAO05] W. Senaratne, L. Andruzzi, , and C. K. Ober. Self-assembled monolayers and polymerbrushes in biotechnology: current applications and future perspectives. *Biomacromolecules*, 6(5):2427–2448, 2005.

[SCL+03] Y.S. Shin, K. Cho, S.H. Lim, S. Chung, S.-J. Park, C. Chung, D.-C. Han, and J.K. Chang. Pdms-based micro pcr chip with parylene coating. *J. Micromech. Microeng*, 13(5):768, 2003.

[SCR+03] L.R. Senesac, J.L. Corbeil, S. Rajic, N.V. Lavrik, and P.G. Datskos. Ir imaging using uncooled microcantilever detectors. *Ultramicroscopy*, 97(1):451–458, 2003.

[Sin17] J.P. Singer. Thermocapillary approaches to the deliberate patterning of polymers. *Journal of Polymer Science Part B*, 2017.

[SOKH08] H.W. Siesler, Y. Ozaki, S. Kawata, and H.M. Heise. *Near-infrared spectroscopy: principles, instruments, applications*. John Wiley and Sons, 2008.

[STARU01] E. Schoffer, T. Thurn-Albrecht, T.P.and Steiner Russell, and U. Electrohydrodynamic instabilities in polymer films. *EPL (Europhysics Letters)*, 53(4):518, 2001.

[STK+07] N. Skivesen, A. Têtu, M. Kristensen, J. Kjems, L.H. Frandsen, , and P. I. Borel. Photonic-crystal waveguide biosensor,. *Opt. Express*, 15:3169, 2007.

[SWKa95] Janusz Sadowski, Ilkka W., K.J. Korhonen, and and. Jouko pk peltonen. "characterization of thin films and their structures in surface plasmon resonance measurements.". *Optical engineering*, 34(9):2581–2587, 1995.

[TFTU09] M.F. Toy, O. Ferhanoglu, H. Torun, and H. Urey. Uncooled infrared thermomechanical detector array: Design, fabri-cation and, 2009.

[TPF06] K.A. Tetz, L. Pang, and Y. Fainman. High-resolution surface plasmon resonance sensor based on linewidth-optimized nanohole array transmittance. *Opt. Lett*, 31(10):1528–1530, 2006.

[Tre11] R. Trebino. Measuring the seemingly immeasurable. *Nat. Photonics*, 5:189–192, 2011.

[TS03] G. Turhan-Sayan. Temperature effects on surface plasmon resonance: Design considerations for an optical temperature sensor. *J. Lightwave Technol*, 21(3):805, 2003.

[VM10] M. Vollmer and K.-P. Möllmann. *Infrared Thermal Imaging: Fundamentals, Research and Applications*. John Wiley and Sons, 2010.

[VSW91] R.G. Vaughan, N.L. Scott, and D.R. White. The theory of bandpass sampling. *IEEE Trans. Signal Process*, 39:1973–1984, 1991.

[Wan11] Zengbo Wang. Optical virtual imaging at 50 nm lateral resolution with a white-lightnanoscope. *Nature communications*, 2:218, 2011.

[WDBW+06] H. Wen, T. DeCory, W. Borejsza-Wysocki, , and R. Durst. *Investigation of NeutrAvidin-tagged liposomal nanovesicles as universal detection reagents for bioanalytical assays,*. Talanta, 2006.

[Wed14] H.M.J.M. Wedershoven. Infrared laser induced rupture of thin liquid films onstationary substrates. *Applied physics letters*, 104(5):054101, 2014.

[WK88] B.Rothenhausler W. Knoll. Surface plasmon microscopy. *Nature*, 332(6165):615, 1988.

[WO14] C.L. Wong and M. Olivo. Surface plasmon resonance imaging sensors. *A Review. Plasmonics*, 9(4):809–824, 2014.

[WZW95] W.E. Wallace, J.H.Van Zanten, , and W. L. Wu. Influence of an impenetrable interface on a polymer glass-transition temperature. *Physical review*, 52(4):3329, 1995.

[Yea96] E.M. Yeatman. Resolution and sensitivity in surface plasmon microscopy and sensing. *Biosensors and Bioelectronics*, 11(6-7):635–649, 1996.

[YRKF94] Rachel Yerushalmi-Rozen, Jacob Klein, , and Lewis J. Fetters. Suppression of rupture in thin nonwetting liquid films. *Science*, 263(5148):793–795, 1994.

[YTG+06] K.G. Yager, O.M. Tanchak, C. Godbout, H. Fritzsche, , and C.J. Barrett. Photomechanical effects in azo-polymers studied by neutron reflectometry. *Macromolecules*, 39(26):9311–9319, 2006.

[YY06] A. Yariv and P. Yeh. Photonics: Optical electronics in modern communications (the oxford. In *Series in Electrical and Computer Engineering)*. Oxford University Press, Inc, 2006.

[YZR+14] F. Yi, H. Zhu, J.C. Reed, A.Y. Zhu, and E. Cubukcu. Thermoplasmonic membrane-based infrared detector. *IEEE Photonics Technol. Lett*, 26(2):202–205, 2014.

[Zan13] A. Zangwill. *Modern electrodynamics.* Cambridge University Press, 2013.

[ZBC+14] A. Zanella, N. Bui, A. Castellani, L. Vangelista, and M. Zorzi. Internet of things for smart cities. *IEEE Internet Things J*, 1:22–32, 2014.

[ZIM+13] H. Zhu, S.O. Isikman, O. Mudanyali, A. Greenbaum, and A. Ozcan. Optical imaging techniques for point-of-care diagnostics. *Lab. Chip*, 13:51–67, 2013.

[ZOY14] J. Zhu, S.K. Ozdemir, and L. Yang. Infrared light detection using a whispering-gallery-mode optical microcavity. *Appl. Phys. Lett*, 104(17):171114, 2014.

[ZYC12] H. Zhu, F. Yi, and E. Cubukcu. Nanoantenna absorbers for thermal detectors. *IEEE Photonics Technol. Lett*, 24(14):1194–1196, 2012.

[ZZLS06] Z. Zhang, P. Zhao, P. Lin, and F. Sun. *Thermo-Optic Coefficients of Polymers for Optical Waveguide Applications*, volume 47. Polymer, 2006.